



Cubic elasticity of porous materials produced by additive manufacturing: experimental analyses, numerical and mean-field modelling

Katarzyna Kowalczyk-Gajewska¹ · Michał Maj¹ · Kamil Bieniek¹ · Michał Majewski¹ · Kamil C. Opiela¹ · Tomasz G. Zieliński¹

Received: 13 September 2023 / Revised: 23 October 2023 / Accepted: 27 November 2023
© The Author(s) 2024

Abstract

Although the elastic properties of porous materials depend mainly on the volume fraction of pores, the details of pore distribution within the material representative volume are also important and may be the subject of optimisation. To study their effect, experimental analyses were performed on samples made of a polymer material with a predefined distribution of spherical voids, but with various porosities due to different pore sizes. Three types of pore distribution with cubic symmetry were considered and the results of experimental analyses were confronted with mean-field estimates and numerical calculations. The mean-field ‘cluster’ model is used in which the mutual interactions between each of the two pores in the predefined volume are considered. As a result, the geometry of pore distribution is reflected in the anisotropic effective properties. The samples were produced using a 3D printing technique and tested in the regime of small strain to assess the elastic stiffness. The digital image correlation method was used to measure material response under compression. As a reference, the solid samples were also 3D printed and tested to evaluate the polymer matrix stiffness. The anisotropy of the elastic response of porous samples related to the arrangement of voids was assessed. Young’s moduli measured for the additively manufactured samples complied satisfactorily with modelling predictions for low and moderate pore sizes, while only qualitatively for larger porosities. Thus, the low-cost additive manufacturing techniques may be considered rather as preliminary tools to prototype porous materials and test mean-field approaches, while for the quantitative and detailed model validation, more accurate additive printing techniques should be considered. Research paves the way for using these computationally efficient models in optimising the microstructure of heterogeneous materials and composites.

Keywords Pore configuration · Anisotropy · Elasticity · Micro-mechanics · Additive manufacturing

1 Introduction

In view of their microstructure, heterogeneous materials can be divided into those with a random but statistically homogeneous microstructure and those with a periodic one. In the first case, the microstructure can be characterised by a set of statistical distribution functions of microstructural parameters, e.g. size and shape distributions or various n -point correlation functions [1]. Among such materials, there are

natural (e.g. metal polycrystals) and synthetic (e.g. composites) materials. However, even for the synthetic materials, the microstructure morphology, as described by the mentioned parameters, can only be controlled to a limited extent. In the second case, the so-called unit cell representing the microstructure can be easily defined, as its periodic multiplication fills the entire volume of the material. Materials with this type of microstructure are mainly synthetic-like metamaterials produced by additive manufacturing (AM). In this case, an almost full control over the microstructure morphology is achieved. Assuming that the link between the microstructure features and the effective mechanical properties is known, this paves the way for the optimal material-by-design techniques.

Knowledge about homogenised mechanical properties of multiphase materials and metamaterials has application in

✉ Katarzyna Kowalczyk-Gajewska
kkowalcz@ippt.pan.pl

¹ Institute of Fundamental Technological Research, Polish Academy of Sciences, Pawińskiego 5B, 02-106 Warsaw, Poland

many areas of research. For example, modelling acoustic wave propagation in poroelastic media requires the effective Young's modulus and Poisson's ratio of a material [2]. In material science, effective elastic properties are determined; e.g. to assess stiffness and strength of bio-scaffolds [3] and lightweight load-carrying cellular microstructures such as rigid closed-cell polyisocyanurate foams [4].

Various rapid prototyping techniques that utilise the principle of additive manufacturing, commonly known as three-dimensional (3D) printing, have allowed experimental study of both closed- and open-porosity systems of a predefined form from the mechanical point of view. The issue of uniform and irregular porosity present in 3D printed components is reviewed in [5], whereas a general characterisation of additively manufactured polymers is made in [6]. In [7], authors experimentally studied the influence of infill patterns on the mechanical properties of 3D printed samples subject to uniaxial tensile tests. As expected, several microstructures of the same porosity but distinct internal topology evinced different effective elastic properties. Highly porous periodic geometries have also been investigated [8–10]. Their superior performance for a relatively low weight per volume when compared to their bulk counterparts was reported.

Classical mean-field models based on the inclusion-matrix concept, which exploit the well-known solution by Eshelby [11], are able to account only for the average ellipsoidal shape of inclusions (here pores) and volume fraction effects. Among those well-established methods are the Mori–Tanaka (MT) model, the self-consistent (SC) and generalised self-consistent schemes, or differential and incremental schemes; cf. [12]. More elaborate models allow for taking into account the secondary factors influencing the effective properties, namely packing and size effects. One may mention here the formulations which use the coated inclusion concept [13, 14], also applicable to nanocrystalline materials [15], the imperfect 2D interface [16] or the morphologically representative pattern (MRP) approach, proposed in [17], validated in [18], and recently extended in [19]. One of the important limitations of the above schemes is that the delivered effective properties remain isotropic as long as inclusions or pores are spherical and phase properties are isotropic, no matter how ordered is their distribution within the matrix. This limitation is overcome by variational approaches developed, e.g., in [20] and used later for elastic–plastic or viscoelastic media in [21] and [22], respectively. The authors apply the phase distribution functions and the effective coated inclusion for which the shape of coating reflects the symmetry of a particle distribution pattern. The drawback of these methods is the fact that not all eight classes of elastic anisotropy can be described in this way. For example, the cubic symmetry is excluded, since the obtained effective ellipsoid is reduced to a sphere in this case, and thus, the resulting effective stiffness is isotropic [23]. Next

to the variational approach, analytical solutions for periodic particle distributions have been obtained, usually in terms of series [24, 25], using the unit cell methodology for the selected microstructures [26, 27], and more recently for an arbitrary space distribution of particles [28]. While these solutions can describe any elastic anisotropy resulting from the space distribution of inclusions, the use of an advanced mathematical apparatus and special functions is necessary. An interesting alternative, which avoids the drawbacks of the above-mentioned methods, is the interaction (cluster) model based on the approximated solution of the multiple inclusion problem in the elastic or thermoelastic infinite matrix, as proposed in [29] and [30], respectively. This last approach is described in more detail and used as the main mean-field method in the present study.

The focus of the present paper is on materials with closed porosity produced using AM techniques. The questions we try to answer are (i) what is the influence of morphological features on the effective properties of porous materials, and (ii) how to successfully and efficiently account for this effect in the micromechanical mean-field models to predict overall elastic properties. The proposed micromechanical solution is verified with numerical and experimental results.

The paper consists of four main parts, including this introduction. The following section presents the production of samples with predefined microstructure morphology by 3D printing (Sect. 2.1), as well as its experimental identification in terms of elastic Young's modulus (Sect. 2.2). Section 3 is divided into five subsections. The first one reviews the general formulation of the micromechanical cluster model and provides its specification as well as the parametric study related to porous materials with a cubic distribution of spherical pores. Section 3.2 focuses on the principles of the unit cell numerical analyses of 3D printed materials, intended to provide reference solutions (i.e., the results of relevant numerical experiments) for the cluster model, namely the material response under hydrostatic compression and isochoric tension studied in Sects. 3.3 and 3.4, respectively, while Sect. 3.5 compares the results of the mean-field and numerical analyses with experimental data obtained for uniaxial compression. Concluding remarks are given in Sect. 4.

2 Production and testing of porous samples with cubic symmetry

2.1 Geometry, additive manufacturing, and quality of porous samples

The research was carried out both experimentally and computationally. Experimental analyses were performed on 3D printed porous samples with periodic microstructures,

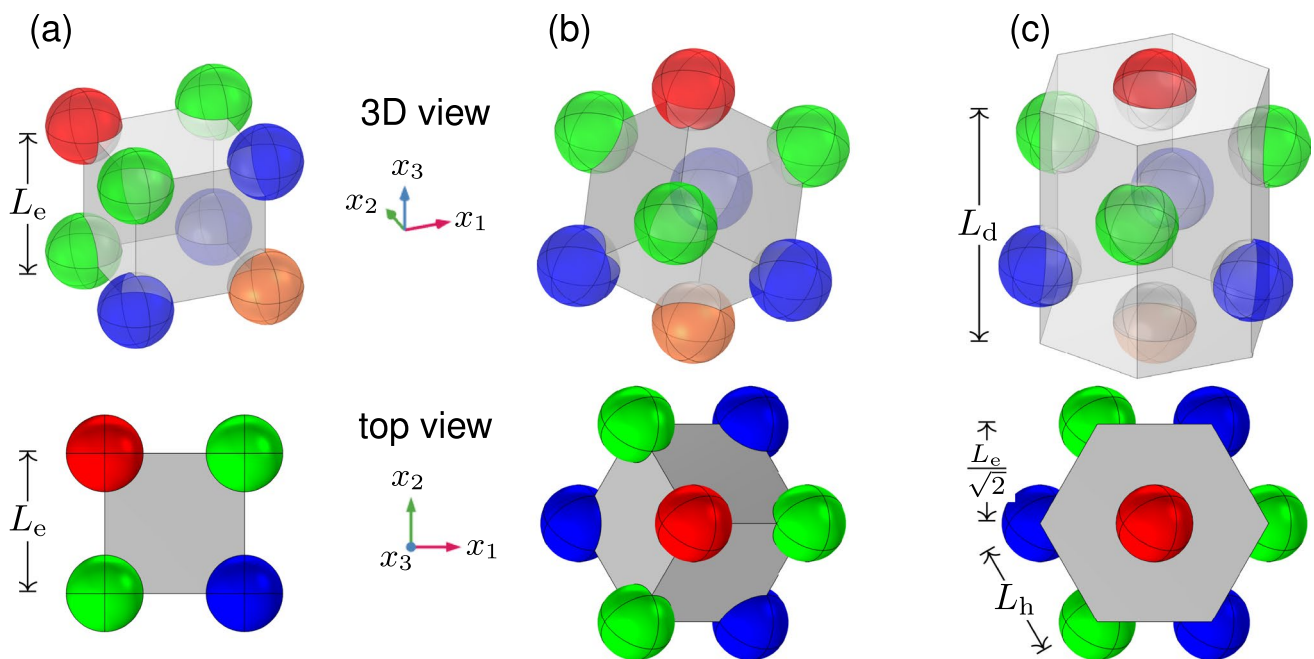


Fig. 1 Two orientations of the RC arrangement of spherical pores or inclusions: **a** for the x_3 -axis along the edge of the cube, and **b, c** for the x_3 -axis along the cube's diagonal; as well as two corresponding unit cells in the form of: **(a, b)** a cube, and **c** a hexagonal prism

for which the required periodic geometries had to be generated first. The essential parts of these geometries were also used for parametric finite-element (FE) analyses. The studied materials have single porosity meaning that the matrix is essentially solid. Moreover, their porosity is closed and composed from identical spherical pores which are not connected. Three types of pore distribution based on the well-known cubic symmetry systems are considered, namely: the regular cubic (RC), body-centred cubic (BCC), and face-centred cubic (FCC) arrangements of spherical pores. Diagonally oriented versions of these pore distributions are also used for the investigation of elastic anisotropy, although only one of them, namely the diagonally oriented RC system was included in the experimental analyses. The reason for this choice will become clear once the modelling framework and its predictions are presented (see Sect. 3). Representative unit cells associated with the three cubic systems as well as the two orientations are explained below along with how these cells are used to 3D print porous samples. The qualities of the samples, and in particular the actual pore shapes and sizes, are discussed at the end of this section, while the results of experimental analyses are given in Sect. 2.2.

Figure 1(a) shows a representative cubic cell of a periodic material with identical spherical inclusions or pores—represented by coloured spheres—in the RC arrangement. This work essentially deals with porous materials, which means that the volumes occupied by the spheres are removed yielding a representative unit cell similar to the one used for 3D printing and FE calculations, as seen further below for

the RC case in Figs. 3 and 9, respectively. The edge length of the cube is L_e , so the cubic cell volume is $V = L_e^3$, while the inclusion or pore diameter is denoted by D_p . For the RC arrangement, there is only a single spherical inclusion or pore in such a cubic cell—note that in Fig. 1(a), only one-eighth of each of the eight identical spheres belongs to the cube—so the inclusion or pore volume is $V_p = \frac{\pi}{6} D_p^3$, while the matrix or solid part volume is $V_m = V - V_p$. The inclusion or void volume fraction, i.e. the porosity in the latter case, equals $f = V_p/V = \frac{\pi}{6} (D_p/L_e)^3$, and the matrix or solid volume fraction is $f_m = 1 - f$. Recall that in the BCC arrangement, an extra sphere is added in the centre of the cube and then $V_p = \frac{\pi}{3} D_p^3$ and $f = \frac{\pi}{3} (D_p/L_e)^3$, while three complete spheres are added in the FCC arrangement (i.e. half a sphere per the cube's face) which results in $V_p = \frac{2\pi}{3} D_p^3$ and $f = \frac{2\pi}{3} (D_p/L_e)^3$. Consequently, for the same pore diameter, the porosities for the BCC and FCC cases are, respectively, two and four times greater than for the RC case. Figure 2 shows how the porosity (and thus, the solid volume fraction) changes as the pore diameter increases relative to the cell size. The maximum values of closed porosity and relative pore size are summarised in the table in this figure. Obviously, all these results strongly depend on the pore distribution.

The cubic cell can be used for a numerical test of uniaxial compression or tension (see Sect. 3.5) of such composite or porous materials along any of the cube edges, to determine the corresponding Young's modulus \bar{E}_e and

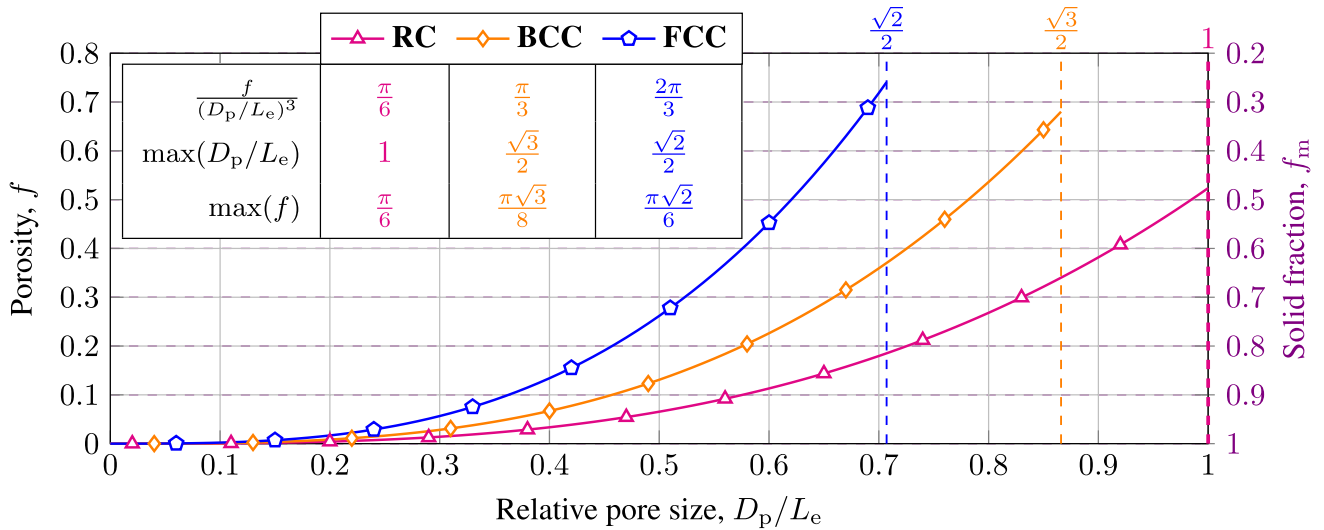


Fig. 2 Porosity (i.e. void fraction) and solid volume fraction vs. the pore diameter-to-cell ratio, for three cubic arrangements of spherical pores

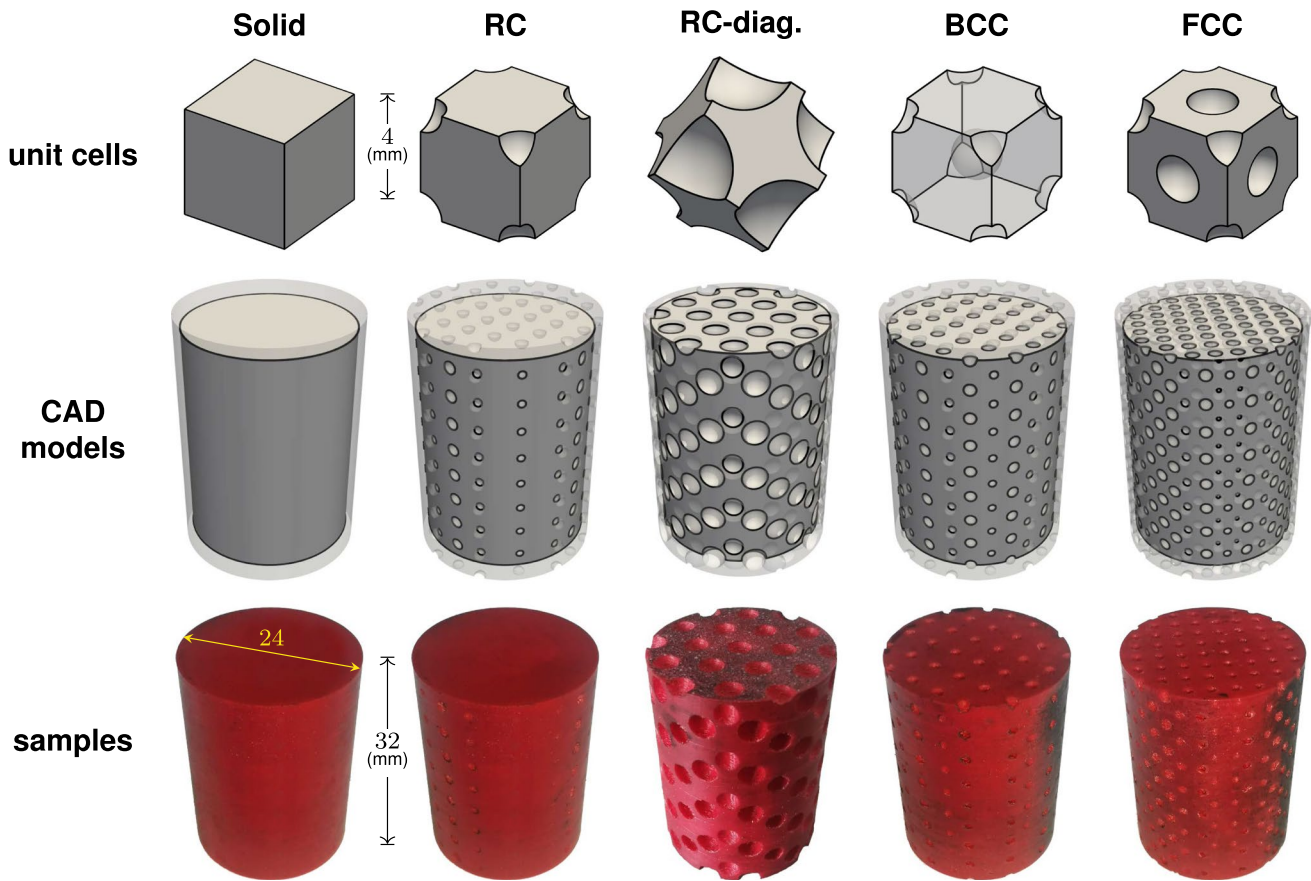


Fig. 3 Cubic unit cells and CAD models as well as 3D printed and machined samples with cubic distributions of spherical pores for $D_p = 1.7$ mm (RC, BCC, and FCC) and $D_p = 3.5$ mm (RC-diag.), or without pores (Solid)

Poisson’s ratio $\bar{\nu}_e$. On the other hand, a *direct* numerical or physical test to determine \bar{E}_d , i.e. the Young’s modulus

along the direction parallel to the diagonal of the cube, requires a representative cell that allows to realise uniaxial

compression or tension along such a direction, e.g. the one determined by the centres of red and orange spheres shown in Fig. 1. The length of the diagonal is $L_d = L_e\sqrt{3}$ and this is the largest distance between two pores (inclusions) in the RC arrangement inside the representative cell. To place the diagonal connecting two spheres along the x_3 -axis of the system of reference set at the centre of the cube, the cube can first be rotated by an angle of $\pi/4$ around the x_1 -axis, and then around the x_2 -axis by an angle equal to $\arccos(\sqrt{2/3})$. The rotated cube is shown in Fig. 1(b) where the red sphere is at the top, with its centre at $x_3 = L_d/2$ on the x_3 -axis, three green spheres are all on the same level that is situated below the red sphere, while three blue spheres are even lower, i.e. at a certain but the same level above the orange ball centred at $x_3 = -L_d/2$ on the x_3 -axis. When viewed from above, it is easy to see that the projections of the centres of green and blue spheres on a plane perpendicular to the x_3 -axis form the corners of a regular hexagon, which is the base of a hexagonal prism visualised in Fig. 1(c). The edge length of the hexagonal base is $L_h = L_e\sqrt{2/3}$ and the height of the prism is L_d , since the red and orange spheres are at the centres of opposite bases. The volume of the hexagonal prism equals $\frac{3\sqrt{3}}{2}L_h^2L_d = 3L_e^3$, which is three times the volume of the cubic cell, but it contains three complete spheres so obviously the fractions remain unchanged. Moreover, when additional spheres—required by the BCC or FCC arrangements—are included in the transformation based on the rotation around the axes of the centred reference system, they reappear in the hexagonal prisms to form a consistent unit cell. Note, however, that some of these additional spheres originally belong to the adjacent cubic cells. In this work, the spheres are voids (i.e. pores), so the corresponding porous cubes and hexagonal prisms will be provided in Sect. 3.2 for the three cubic arrangements of spherical pores. Additionally, the cubic symmetry will be used to select smaller yet fully representative fragments of these unit cells suitable for FE calculations. The porous unit cells were also used to generate geometries for 3D printing as described below.

Nearly 20 cylindrical samples of diameter 24 mm and height 32 mm were produced for uniaxial compression testing. Three of these samples are solid cylinders (see the left-most photo in the bottom row of Fig. 3), but the remaining ones are porous, with designed periodic systems of closed spherical pores. In principle, their individual microstructures were constructed from periodic cubic cells with the RC, BCC, or FCC arrangements of spherical pores. In addition, a diagonally oriented version of the RC system (i.e. ‘RC-diag.’) was also used to produce samples, as it was expected that in this case, the uniaxial compression tests should provide Young’s moduli that are clearly different to those obtained from the standard compression ‘along the edge’.

One example for each unit cell—generated for the specified nominal pore size—is depicted in the top row of Fig. 3. Basically, five nominal values of pore diameters were used to create geometries used for 3D printing, namely $D_p = 1.7, 2.15, 2.5, 3.1, \text{ and } 3.5$ mm, with the nominal unit cell size of 4 mm. Note, however, that the BCC and FCC arrangements of *closed* pores do not allow D_p/L_e ratios larger than $\sqrt{3}/2$ and $\sqrt{2}/2$, respectively, see Fig. 2. Therefore, in these cases, the largest, or respectively, two largest values were excluded from the above set of nominal pore diameters. On the other hand, only the two largest diameters were used to produce samples with pores arranged in the diagonally oriented RC system, as we expected that the elastic properties of samples with smaller pores should not differ significantly, regardless of whether the same cubic arrangement is diagonally oriented or aligned along the edge of the unit cell.

All designs of the cylindrical samples were created in FreeCAD [31], an open-source computer-aided design (CAD) software, by cutting cylindrical shapes out of three-dimensional regular arrays of the respective unit cells. For each microstructure, the central axis of the cylinder was aligned parallel either to the edge of the unit cell cube (the RC, BCC, and FCC cases) or to its diagonal (the RC-diag. case). About 2 mm larger dimensions of the cylinder diameter and height than the final required values of 24 mm and 32 mm, respectively, were assumed in the CAD models of cylindrical specimens to enable their machining to precise external shape and size after the additive manufacturing process is completed. The CAD models used to 3D print porous samples with the nominal pore diameter $D_p = 1.7$ mm (the RC, BCC, and FCC arrangements) and $D_p = 3.5$ mm (the RC-diag. case) are depicted in Fig. 3 (middle row) along with the corresponding manufactured and machined specimens (bottom row).

In addition to the porous cylindrical samples, three solid cylinders of the same diameter and height were produced. One of these solid samples is shown in Fig. 3. They served the purpose of reference specimens for the experimental determination of the elastic properties of the 3D-printed solid material, and thus the matrix material of the porous samples. Similarly to the porous cylinders, the CAD model of the solid cylinder has an extra volume around it, which is removed at the last fabrication stage by means of conventional subtractive methods such as turning with a lathe. This machining allowance is shown as transparent regions in all CAD models; see Fig. 3 (middle row).

The samples were additively manufactured using the aforementioned CAD models and the fused deposition modelling (FDM) technology [32]. This is a rapid prototyping method in which a thermoplastic filament is heated up to the melting point and extruded layer-by-layer to form the desired object. The process is guided by an executive code that describes its parameters like movement speeds,

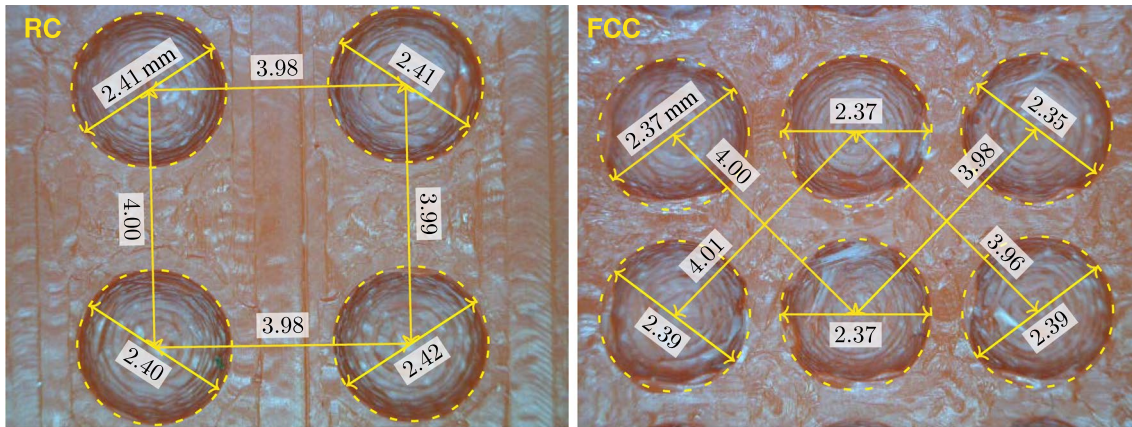


Fig. 4 Typical manufacturing tolerances (dimensions in mm) at the top surfaces of two exemplary RC and FCC porous samples with the nominal pore size $D_p = 2.5$ mm and $L_e = 4$ mm, before being machined on a lathe

temperatures, and current positions of the nozzle with respect to the build platform. In this research, the machine instruction code was generated by the Ultimaker Cura 4.8.0 software and run on the FlashForge Creator Pro device operating in the FDM technology. The acrylonitrile butadiene styrene (ABS) polymer material (rigid.ink) was used for 3D printing at a temperature of 235 °C on a platform kept at a constant temperature of 95 °C to guarantee good adhesion of the first 3D-printed layer and therefore the whole object. The polymer material was pushed through a copper nozzle with a 0.4-mm round opening to create individual layers of height equal to 0.08 mm. Afterwards, when the manufacturing ended and a sample was ready, its lateral, top, and bottom sides were machined on a lathe, resulting in high accuracy of its outer dimensions and improved cylindrical shape. Several final specimens are displayed in Fig. 3 (bottom row). As the thermoplastic filament is simply melted during the 3D printing process, its mechanical and geometrical properties remain practically the same over time, since a sample is cooled down to room temperature. Selected values of nominal pore diameters mentioned before guarantee manufacturability of a sample in the FDM technology. The smallest spherical pore that can be fabricated with sufficient quality in the FDM technology should have about 1.5 mm in diameter. As concerns the largest pore diameter, one needs to subtract at least the minimal manufacturable wall thickness equal to the nozzle size (0.4 mm) from the theoretically allowable D_p , to enforce full separation of pores. In both cases, it is also necessary to take into account little shrinkage (about 0.1 mm for diameters) of the ABS material after finishing the 3D printing process to eventually get the nominal diameter values given above.

No production technology allows to obtain exactly the same geometry as in the design. To investigate the quality of the obtained microstructures, the manufactured samples were examined under a digital microscope before being

machined on a lathe. The results of measurements of pore diameters and distances for two exemplary porous specimens with $D_p = 2.5$ mm are shown in Fig. 4. Despite relatively regular spherical pore shapes, especially for the RC and BCC samples, the conducted study reveals that the specimens have microstructures with slightly *smaller* characteristic dimensions than the values in their respective CAD models. Namely, the top-surface pore diameters have about 2.39 mm on average thus are smaller than 2.5 mm, and the average distance between the top-surface pores (i.e. the unit cell size) is approximately 3.98 mm, hence subtly smaller than 4 mm. This is because the material tends to shrink when cooled down to room temperature. On the other hand, the real pore diameters in the samples are smaller than nominal primarily because they are determined by the outer surfaces of individually extruded material paths formed by pushing material through a round nozzle tip at certain flow rate. If the flow rate is not perfectly matched to the nozzle size and process parameters, the paths are typically wider than the nozzle orifice or may be discontinuous and insufficient to result in a good-quality printout. To ensure no porosity in the sample skeleton, a slightly higher than optimal flow rate was used, which, combined with the offset between the boundaries of the CAD model and the centreline of the nozzle perimeter movement equal to its radius and present in the machine code, led to an overall diameter reduction of 0.11 mm on average in the manufactured object. However, this deviation from the nominal value is considered the same for every diameter D_p , since the introduced offset depends solely on the nozzle radius, and process parameters were not modified sample-wise. The observed discrepancies were taken into account when plotting the *measured* values of Young's modulus with respect to the relative pore size D_p/L_e (see Figs. 13, 14, 15, 16 and 17 in Sect. 3). It is then assumed that the actual value of pore diameter in a 3D printed sample is 0.11 mm smaller than the nominal value, and the edge of



Fig. 5 Experimental setup with one of the porous samples inserted in between two hydraulic grips with adjustable clamping force

the cubic cell is 3.98 mm instead of 4 mm. For convenience, Table 3 in the next section contains information about the nominal and actual, i.e. measured, values of average pore diameters for each produced porous sample that was used to test the elastic properties.

2.2 Mechanical properties' measurements

The effective elastic moduli of cylindrical samples with different porosity and pore distributions created using the FDM additive manufacturing process were determined during compression tests. Before the test, an appropriate part of the surface of each sample was covered with graphite and small dots of white paint to perform digital image correlation (DIC) analysis. The displacement-controlled tests were conducted using the MTS 858 hydraulic testing machine. The experimental setup is presented in Fig. 5.

The displacement rate of 0.032 mm/s was used. Taking into account the sample geometry, this corresponds to strain rate equal to 10^{-3}s^{-1} . The initial force $F = 1000$ N, corresponding to the initial nominal stress of approximately 2 MPa, was applied to perfectly align the sample and avoid undesirable effects resulting from manufacturing imperfections (surface imperfections, in particular). During deformation, both the compressive force evolution and a sequence of images of the tested sample were recorded simultaneously. The images were taken using the pco.edge 5.5 sCMOS camera with picture taking frequency of 30 Hz. Basic camera settings are presented in Table 1.

Table 1 Settings of the pco.edge 5.5 sCMOS camera applied during experiments

Resolution (pixel)	1080 × 1280
Exposure time (ms)	3
Pixel size (μm)	25
Binning	2 × 2
Taking frequency (Hz)	30

Table 2 Parameters used for the DIC analysis

Subset type	Circle
Subset radius (pixel)	10
Correlation criterion	ZNCC
Interpolation type	bicubic
Update of ref. image	no update

Using the obtained image sequences and the 2D digital image correlation algorithm, the displacement of points lying on the generatrix of the cylindrical samples were determined. The detailed description of the used self-implemented DIC algorithm as well as the analysis of its accuracy are presented in [33] and [34], respectively. The parameters used in the DIC analysis are listed in Table 2.

The so-called 'virtual extensometer' was used to determine the mean strain in the loading direction. The base of the 'virtual extensometer' was the same for each sample and was equal to 27 mm; it was set 2.5 mm from the grips of testing machine at each side) to avoid boundary effects, see Fig. 6. This base (cf. the red vertical line in Fig. 6 spans almost eight unit cells for the microstructures tested along the edge direction. In the case of microstructures tested along the diagonal direction, such base spans four ('rotated') unit cells. Such selection of the cylindrical sample size and the 'virtual extensometer' ensures that the measured values can be treated as corresponding to the effective material properties assessed in the mean-field modelling. The verification of this, which preceded the sample preparation and experiment design, was performed by comparing the results of FE simulations of the compression test on the full cylindrical sample with the corresponding results for unit cells under the boundary conditions as described in Sect. 3.5. Moreover, to verify measurement repeatability, three tests were performed for every considered microstructure. The variability of the obtained values of Young's modulus were negligible for the given sample.

The linear regression of the obtained nominal stress vs. engineering strain dependence was performed and the effective Young's modulus was determined as the slope of the fitted line as demonstrated in Fig. 7. For the regression model, the maximum number of points was used, usually more than 100 data points, for which the coefficient of determination $R^2 \geq 0.999$. Careful observation of the deformation of pores

Fig. 6 One of the samples with the applied graphite layer for the DIC analysis and the position of the 'virtual extensometer'

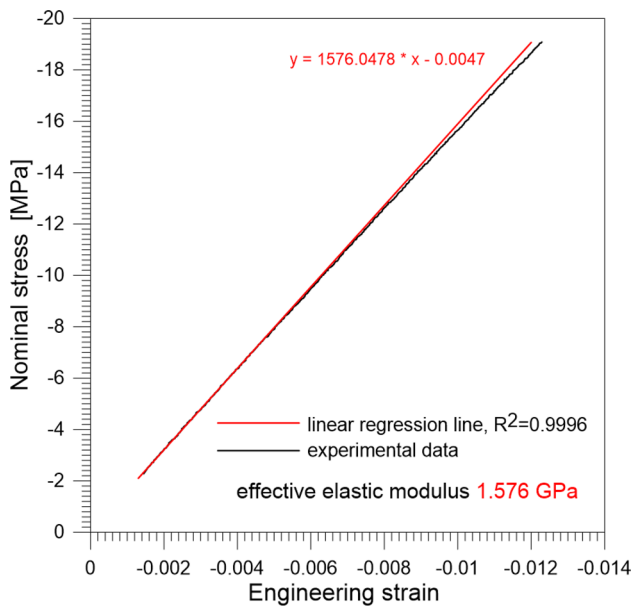
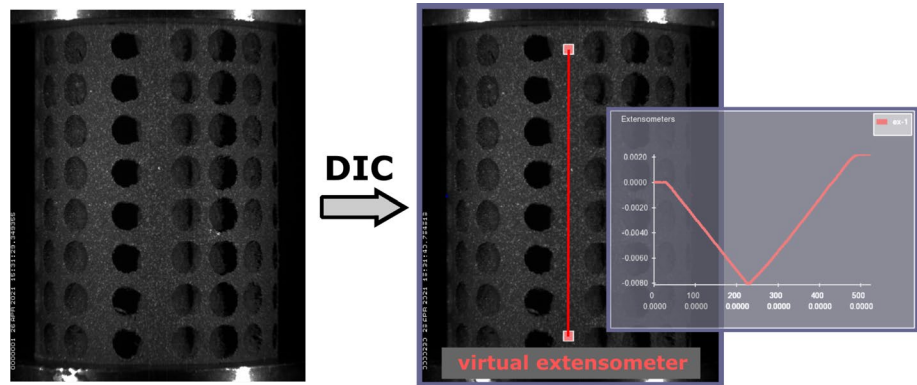


Fig. 7 Evaluation of the effective Young's modulus based on the linear regression for a single sample

and surrounding material confirmed that—within the considered displacement range—the sample response remains linear and local buckling is avoided. Table 3 collects the obtained results for all tested geometries. In the table, the compression test direction is specified in relation to the cubic unit cell of the porous microstructure.

Additionally, the variation of Young's modulus for different samples of the same predefined geometry was checked for the solid cylinders as well as for the selected geometries of relatively large porosities by performing—in each case—the compression experiments on three (essentially 'identical') samples. For those cases, the mean value is given in Table 3 together with the standard deviation.

Moreover, the anisotropy of elastic properties due to the additive manufacturing process was studied on the solid

cubic samples. Using the procedure presented above, the elastic moduli in three orthogonal directions were determined. It was observed that differences between them did not exceed 5% of their mean value. Nevertheless, to minimise the possible influence of the solid matrix anisotropy related to 3D printing on the studied impact of pore distribution, the compression axis coincided with the printing direction for all cylindrical samples, for which the results are presented in Table 3.

3 Mean-field modelling vs. numerical homogenisation and measurements

3.1 Interaction cluster model for porous materials

El Mouden and Molinari [29] proposed a mean-field interaction model (also called "a cluster model") for linear elastic composites. The cluster model was aimed to describe interaction effects between heterogeneities. In this way, the approach accounts for the spatial distribution of inclusions within the material volume, and improves the predictions of classical mean-field schemes for high concentrations. Notice that porous materials studied in the present research are a special case of two-phase materials in which pores are identified as inclusions.

The original formulation of the cluster scheme assumed uniform inclusions of ellipsoidal shape embedded in a uniform matrix of different properties. A representative unit cell with a spatial design of heterogeneities characterising the internal structure of the composite material is assumed, which is next reproduced by periodicity to fill the whole space. Inclusions can be grouped into N families of symmetrically equivalent ones, which, under the uniform strain/stress or periodic boundary conditions imposed at infinity, are supposed to carry the same fields of strain and stress. Within the mean-field approach, the problem reduces to finding the solution providing the mean strain and stress of the representative inclusions. Additively manufactured

Table 3 Results of measurements of the effective Young’s modulus for cylindrical solid and porous samples (average ± standard deviation)

Unit cell type	Compression direction	Nominal pore size (mm)	Actual pore size (mm)	Porosity (%)	Young’s modulus (GPa)	
RC	–	–	–	0.0	2.340 ± 0.058	
		Edge	1.7	1.59	3.3	2.098
			2.15	2.04	7.1	1.950
	Diagonal	2.5	2.39	11.3	1.852 ± 0.073	
		3.1	2.99	22.2	1.721 ± 0.029	
		3.5	3.39	32.4	1.103	
		3.1	2.99	22.2	1.372	
	BCC	Edge	3.5	3.39	32.4	0.922
			1.7	1.59	6.7	2.013
		Edge	2.15	2.04	14.1	1.659
2.5			2.39	22.7	1.428	
FCC	Edge	3.1	2.99	44.4	0.500 ± 0.006	
		1.7	1.59	13.4	1.555	
	Edge	2.15	2.04	28.2	1.032	
		2.5	2.39	45.4	0.562	

Porosity is given for the actual pore size determined from the samples. The nominal pore size is based on the CAD model

microstructures produced within this study are examples of a single family case, so all the pores are symmetrically equivalent. It is worth mentioning that the interaction model was later extended to cover thermoelastic properties [30], conductivity [35], viscoplasticity and elastic-viscoplasticity [36], as well as elastoplasticity [37].

We shortly recall here the basic equations of the elastic interaction cluster model and specify them for the case of porous material. This is a special case of a two-phase medium in which the inclusion phase *p* is made up of a family of equivalent spherical pores embedded in the isotropic matrix phase *m*. The volume fraction of pores, i.e. porosity is denoted by *f*. The matrix phase is governed by the linear elastic law with **C_m** denoting the fourth-order tensor of matrix elastic moduli. Thus, considering the stress **σ_m** and strain **ε_m** averages for the matrix phase, we have¹

$$\sigma_m = C_m \cdot \epsilon_m \tag{1}$$

For pores **σ_p** = **0** and **ε_p** denotes average strain of a pore. Since single family cases are considered, **ε_p** is the same for all the pores in the infinite volume. The whole space is filled by the porous material, and we denote by **Σ** and **E** the macroscopic strain and stress, respectively, which fulfil relations

$$E = f \epsilon_p + (1 - f) \epsilon_m \tag{2}$$

¹ Notation: \cdot denotes a full contraction of the second-order tensor with a fourth order tensor ($C_{ijkl} \epsilon_{kl}$ in components), while \circ , appearing, e.g. in Eq. (4), is a double contraction of two fourth-order tensors ($P_{ijkl} C_{klmn}$ in components)

and

$$\Sigma = (1 - f) \sigma_m \tag{3}$$

Using the Green function technique, the solution of the boundary value problem is obtained in the form of the Lipman–Schwinger–Dyson (LSD) integral equation, see [38]. Then, an approximate solution for the average strain in the pore **ε_p** is derived as

$$\epsilon_p = \epsilon_0 + (P_*^I \circ C_m) \cdot \epsilon_p \tag{4}$$

with

$$P_*^I = -\Gamma^{II} - \sum_{J \neq I} \Gamma^{IJ} = P^0 - \bar{\Gamma}, \tag{5}$$

where the label *I* is given to some arbitrarily selected reference pore. For spherical pores

$$P^0(C_m) = -\Gamma^{II}(\text{sphere}); \tag{6}$$

thus, **P⁰** is the Hill’s polarisation tensor for the isotropic matrix material and a spherical domain. The symbol $\sum_{J \neq I}$ represents summation made by considering all other pores of the family (an infinite number, theoretically). By symmetrical equivalence of all pores, **P^I*** and **Γ̄** are independent of the arbitrary choice of the reference pore *I*.

The fourth-order tensor **Γ^{IJ}** depends on the shape of pores and the relative distance between their centres. It is defined by the integral

Table 4 Specification of the function $\tilde{\Gamma}(f)$ of $\tilde{\Gamma}$ tensor (see Eq. (9)) for three microstructures considered in the present study

Unit cell type	$\tilde{\Gamma}(f)$
RC	$\frac{1}{4\pi} (2.3322 - 2.87075f^{2/3})$
BCC	$\frac{1}{4\pi} (-0.7207 + 0.9037f^{2/3})$
FCC	$\frac{1}{4\pi} (-0.6411 + 0.6896f^{2/3})$

$$\Gamma^{IJ} = \frac{1}{V_I} \int_{V_I} \int_{V_J} \Gamma(\mathbf{r} - \mathbf{r}') d\mathbf{r}' d\mathbf{r} \tag{7}$$

over the domains V_I and V_J occupied by pores I and J , respectively, where the kernel Γ is obtained from the Green functions related to the elastic stiffness \mathbf{C}_m of the reference medium. This integral can be calculated analytically for two spherical inclusions embedded in an isotropic elastic medium, see e.g. [29] or [37]. By introducing the cluster concept and using the properties of Γ^{IJ} tensor, $\tilde{\Gamma}$ is calculated by taking a finite number of terms in the sum in Eq. (5), so we consider interactions between the pores which are included in a sphere of radius R_c whose centre coincides with the one of the reference pore I , namely

$$\tilde{\Gamma} \simeq \tilde{\Gamma}(R_c) = \sum_{J \in C(R_c), J \neq I} \Gamma^{IJ}. \tag{8}$$

It was demonstrated in [29] that for sufficiently large cluster size, the series converges. In [37], the closed-form relations for $\tilde{\Gamma}$ components were found for the RC, BCC, and FCC unit cells of cubic symmetry assuming sufficiently large R_c to reach convergence. Due to properties of the $\tilde{\Gamma}$ tensor, we have: $\tilde{\Gamma}_{1122} = \tilde{\Gamma}_{1212} = -\tilde{\Gamma}_{1111}/2$ and

$$\tilde{\Gamma}_{1111} = \tilde{\Gamma}(f) \frac{f}{G_m(1 - \nu_m)}, \tag{9}$$

where G_m and ν_m are the shear modulus and Poisson’s ratio of the matrix, respectively. The components are found in the basis coaxial with unit cell edges (so cubic symmetry axes). For convenience, the respective specifications of the function $\tilde{\Gamma}(f)$ are collected in Table 4.

In Eq. (4), ϵ_0 is an integration constant that appears in the LSD integral equation. By taking the volume average of the LSD integral equation, in the case of a porous elastic material, the constant is specified as (cf. [29])

$$\epsilon_0 = \mathbf{E} - f\mathbf{P}^0 \circ \mathbf{C}_m \cdot \epsilon_p. \tag{10}$$

Inserting Eqs. (5) and (10) to Eq. (4), the strain localisation equation is found for the average pore strain ϵ_p

$$\epsilon_p = (\mathbb{I} - [(1 - f)\mathbf{P}^0 - \tilde{\Gamma}] \circ \mathbf{C}_m)^{-1} \cdot \mathbf{E} = \mathbf{A}_p \cdot \mathbf{E}, \tag{11}$$

where the fourth-order tensor \mathbf{A}_p is identified as a strain localisation tensor for pores and \mathbb{I} is the symmetrised fourth-order identity tensor. Finally, using Eqs. (1)-(3) and (11), the effective constitutive law for a porous medium with single family of pores can be found, namely

$$\Sigma = \bar{\mathbf{C}} \cdot \mathbf{E} \quad \text{with} \quad \bar{\mathbf{C}} = \mathbf{C}_m - f\mathbf{C}_m\mathbf{A}_p, \tag{12}$$

or equivalently

$$\bar{\mathbf{C}} = \mathbf{C}_m - f(\mathbf{C}_m^{-1} - (1 - f)\mathbf{P}^0 + \tilde{\Gamma})^{-1}. \tag{13}$$

The latter formula demonstrates required symmetry of the effective stiffness (note that $\tilde{\Gamma}$ is symmetric). This tensor has zero isotropic part as defined by the harmonic decomposition of the fourth-order tensor [39, 40]. It is noticed that if $\tilde{\Gamma} = \mathbf{0}$ (i.e., space distribution of spherical pores is perfectly isotropic) then the obtained formulas degenerate to those valid for the classical MT model [41], so it is justified to consider the cluster model as one of the MT-derived methods. Note that the present configuration, i.e., two-phase material and spherical shape of pores, allows us to avoid known limitations of the MT scheme [42], which usually require additional treatment for more complex material configurations [43].

For the produced porous material, due to the space distribution of pores, the overall properties exhibit cubic symmetry if isotropy of the matrix material (solid) is assumed. The elastic stiffness tensor can then be described by three elastic Kelvin moduli [44, 45]: one bulk modulus and two shear moduli. Notice that the anisotropy degree of cubic symmetry materials is quantified by the Zener anisotropy ratio which can be calculated as \bar{G}_d/\bar{G}_e , and equals to one for isotropy. Using Eq. (13), it can be shown that these three material constants are specified as

$$\begin{aligned} \bar{K} &= \frac{1}{3}(\bar{C}_{1111} + 2\bar{C}_{1122}) \\ &= K_m \left(1 - \frac{3f(1 - \nu_m)}{2 + f - \nu_m(4 - f)} \right), \end{aligned} \tag{14}$$

$$\begin{aligned} \bar{G}_e &= \frac{1}{2}(\bar{C}_{1111} - \bar{C}_{1122}) \\ &= G_m \left(1 - \frac{15f(1 - \nu_m)}{7 + 8f - 5\nu_m(1 + 2f) + 45f\tilde{\Gamma}(f)} \right), \end{aligned} \tag{15}$$

$$\begin{aligned} \bar{G}_d &= \bar{C}_{1212} \\ &= G_m \left(1 - \frac{15f(1 - \nu_m)}{7 + 8f - 5\nu_m(1 + 2f) - 30f\tilde{\Gamma}(f)} \right), \end{aligned} \tag{16}$$

where K_m and G_m are the bulk and shear moduli of the matrix, while ν_m is its Poisson’s ratio. Note that the bulk modulus obtained by the cluster model is independent of

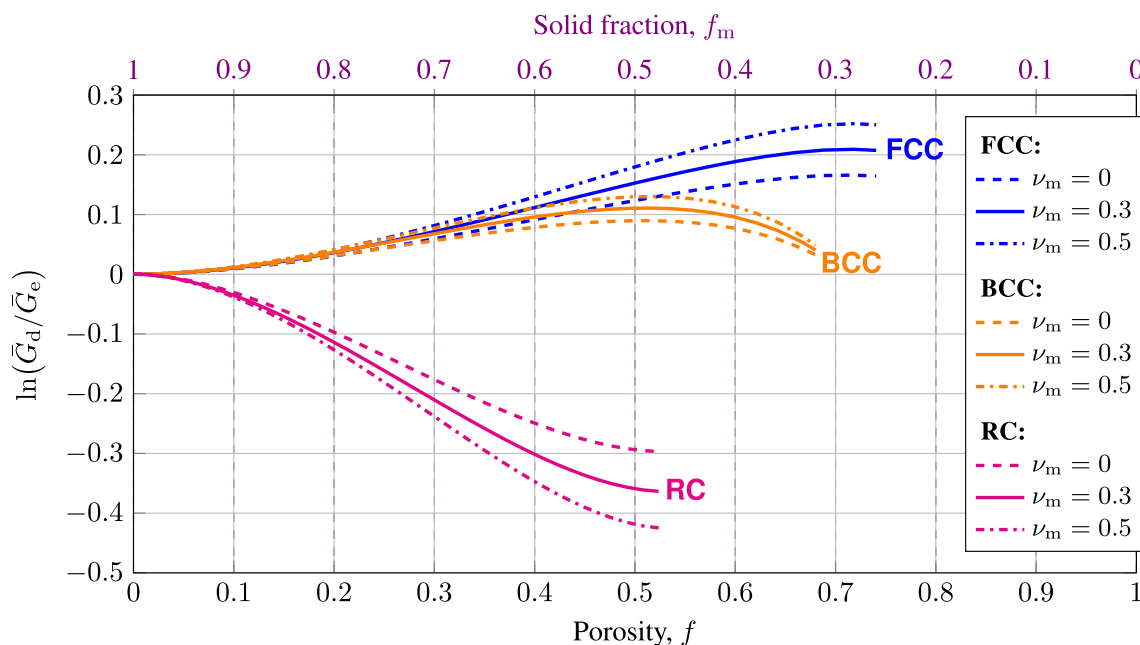


Fig. 8 The natural logarithm of the Zener parameter \bar{G}_d/\bar{G}_e as a function of the pore volume fraction f (or the solid fraction $f_m = 1 - f$) and the Poisson's ratio of the matrix ν_m for three pore arrangements of cubic symmetry

the distribution of pores and is the same as for the classical Mori–Tanaka scheme. On the other hand, the shear moduli \bar{G}_e and \bar{G}_d depend on the space distribution of pores through the presence of the $\bar{\Gamma}$ function in the respective formulas. When the interactions between inclusions are neglected (i.e., for $R_c = 0$ and $\bar{\Gamma} = \mathbf{0}$), then $\bar{G}_e = \bar{G}_d$ and the estimate coincides with the Mori–Tanaka solution. The difference in the two shear moduli results in the anisotropy of the directional Young modulus. In particular, extremal values are obtained for the tension direction along a unit cell edge and along a unit cell diagonal, namely

$$\bar{E}_e = \frac{9\bar{G}_e\bar{K}}{\bar{G}_e + 3\bar{K}}, \quad \bar{E}_d = \frac{9\bar{G}_d\bar{K}}{\bar{G}_d + 3\bar{K}}, \tag{17}$$

and $\bar{E}_e > \bar{E}_d$ when $\bar{G}_e > \bar{G}_d$, and reversely. The values of Young's moduli \bar{E}_e and \bar{E}_d for the produced microstructures have been determined experimentally. One may also calculate two respective Poisson's ratios

$$\bar{\nu}_e = \frac{\bar{E}_e}{2\bar{G}_e} - 1, \quad \bar{\nu}_d = \frac{\bar{E}_d}{2\bar{G}_d} - 1, \tag{18}$$

and check that $\bar{\nu}_e > \bar{\nu}_d$ when $\bar{G}_e < \bar{G}_d$, and reversely.

The logarithm of the Zener parameter as a function of porosity for three pore arrangements considered in this work is plotted in Fig. 8 for three values of Poisson's ratio ν_m : 0, 0.3, or 0.5. It is easy to notice that the anisotropy is qualitatively different for the RC arrangement as compared

to the BCC and FCC arrangements, and it is substantially stronger for RC. Such result is strictly connected with the form of the $\bar{\Gamma}(f)$ function shown in Table 4: the coefficients in the formulae for this function have the opposite sign and their magnitudes are about three times larger for RC than for BCC or FCC. It can also be seen that the degree of anisotropy increases with the increase of the Poisson's ratio of the matrix material, and for a given porosity and pore distribution, the greatest anisotropy is obtained when the matrix material is incompressible, i.e., for $\nu_m = 0.5$.

Formulas (12) and specifically (14)–(16) provided by the mean-field cluster scheme enable straightforward and immediate finding of the effective properties required, e.g., in large-scale simulations of structures made of composites or porous materials. However, their safe use should be preceded by model validation. The necessary verification of the model will now be performed using numerical experiments conducted on unit cells representative for the tested materials, as it is usually done for other mean-field modelling frameworks. The idea of numerical experiment has been developed in [46] and later used on multiple occasions for the validation of the new mean-field proposals, e.g., for the affine model of elastic–viscoplastic heterogeneous medium [47], for the verification of available linearisation procedures proposed to deal with elastic–plastic composites [48], for the additive scheme applied to metal matrix composites exhibiting kinematic hardening under cyclic loading [49] or for the extension of the MRP scheme for an arbitrary shape of inclusions [50]. Note that such virtual experiments

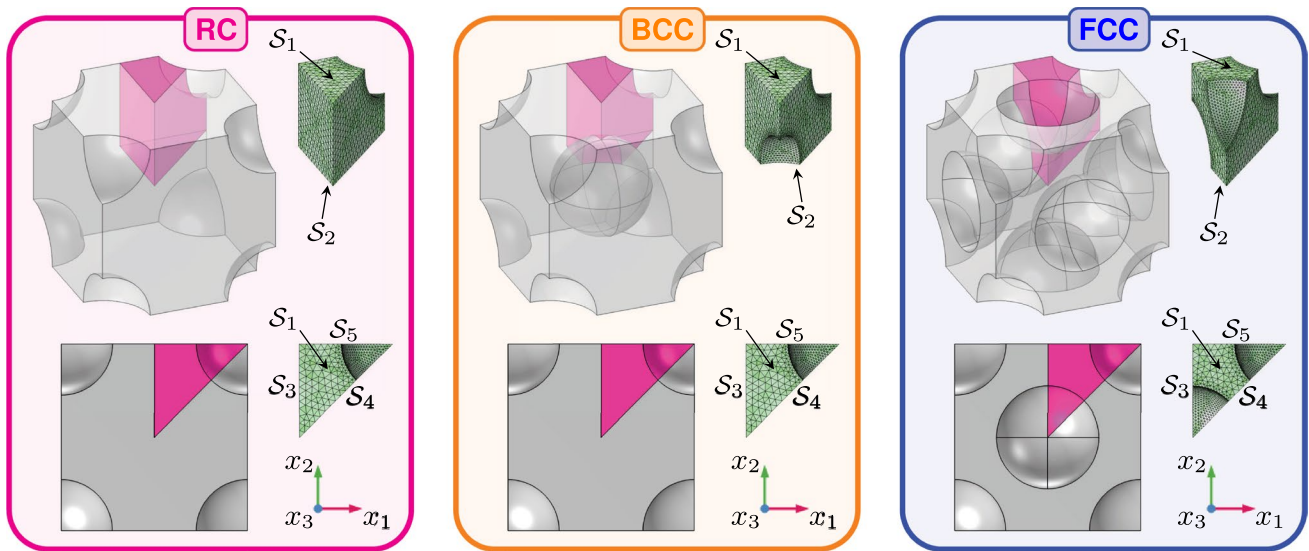


Fig. 9 Cubic unit cells for materials with spherical pores (quasi-isometric and top views for the RC, BCC, and FCC arrangements of pores) with FE-meshed representative segments sliced out by the planes of symmetry

allow full control of the input data such as the properties and constitutive behaviour of the solid material and the microstructure morphology, so the verification concerns solely the micro–macro transition scheme. Finally, some of the cluster model estimates will also be compared with the corresponding experimental findings.

3.2 Representative segments of unit cells for numerical experiments

Figure 9 shows three cubic cells that are representative for porous materials with identical spherical pores in the RC, BCC, and FCC arrangements, respectively. In each case, a transparent quasi-isometric view is shown along with a top opaque view of the cell. The planes of the cubic symmetry group are used to cut out a smaller representative segment, i.e. one-sixteenth of the cube marked within the cell and copied out of it in Fig. 9. The segments shown outside the cubes have FE meshes.

Similarly, the planes of symmetry are also used to select smaller yet fully representative segments of the hexagonal prisms with cubic arrangements of spherical pores shown in Fig. 10. Each segment, i.e. one-sixth of the corresponding porous hexagonal prism, is FE-meshed. Obviously, the FE mesh strongly depends on the relative size of identical spherical pores, so does the geometry of the porous prisms (or cubes) and their representative segments. The particular geometries and FE meshes shown in Figs. 9 and 10 are for $D_p/L_c = 0.55$. However, for example, when the pores in the BCC arrangement of fixed size are enlarged, they eventually remove material around the corners of both hexagonal

bases of the prism, and then, its top view will differ from the top view of the prism with the RC arrangement of pores, though these views are identical for the pore size-to-cell ratio assumed in Fig. 10.

Each of the segments shown in Figs. 9 and 10 has five flat boundary walls denoted by $\mathcal{S}_1, \mathcal{S}_2, \dots, \mathcal{S}_5$. The lateral boundaries $\mathcal{S}_3, \mathcal{S}_4$ and \mathcal{S}_5 are formed by the symmetry planes, while the top face \mathcal{S}_1 and bottom face \mathcal{S}_2 are symmetric boundaries for the segments cut from the cubic cells (see Fig. 9), but periodic boundaries for the segments cut from the hexagonal prisms (see Fig. 10). The remaining boundaries are walls of the spherical pores. The FE mesh there is relatively denser to accurately represent the curvature of the spheres. The boundary conditions applied on the pore walls are always the homogeneous Neumann conditions, i.e., zero surface load, because the pressure of air saturating the pores is negligible.

For the numerical homogenisation procedure discussed below, the following averaging operator $\langle \dots \rangle = \frac{1}{V} \int_V \dots dV$ is used to calculate the average of the stresses and strains over the entire unit cell. Depending upon the orientation, the unit cell is either a cube or a hexagonal prism. It is easy to see that $\langle \dots \rangle = f \langle \dots \rangle_p + f_m \langle \dots \rangle_m$, where $\langle \dots \rangle_p = \frac{1}{V_p} \int_{V_p} \dots dV$ is the averaging operator over the inclusion subdomain in a unit cell, while $\langle \dots \rangle_m = \frac{1}{V_m} \int_{V_m} \dots dV$ is the averaging operator over the matrix. Recall that the inclusions are voids, i.e. pores, and it is assumed that the pores do not sustain any stresses, i.e. $\langle \sigma_{ij} \rangle_p = 0$, so the averaged stress can be calculated for a unit cell of porous material as $\langle \sigma_{ij} \rangle = f_m \langle \sigma_{ij} \rangle_m$, i.e. by averaging only over the solid subdomain, and in practice, due to all symmetries, the averaging takes place over a representative segment of a given cell (see FE meshes in Figs. 9

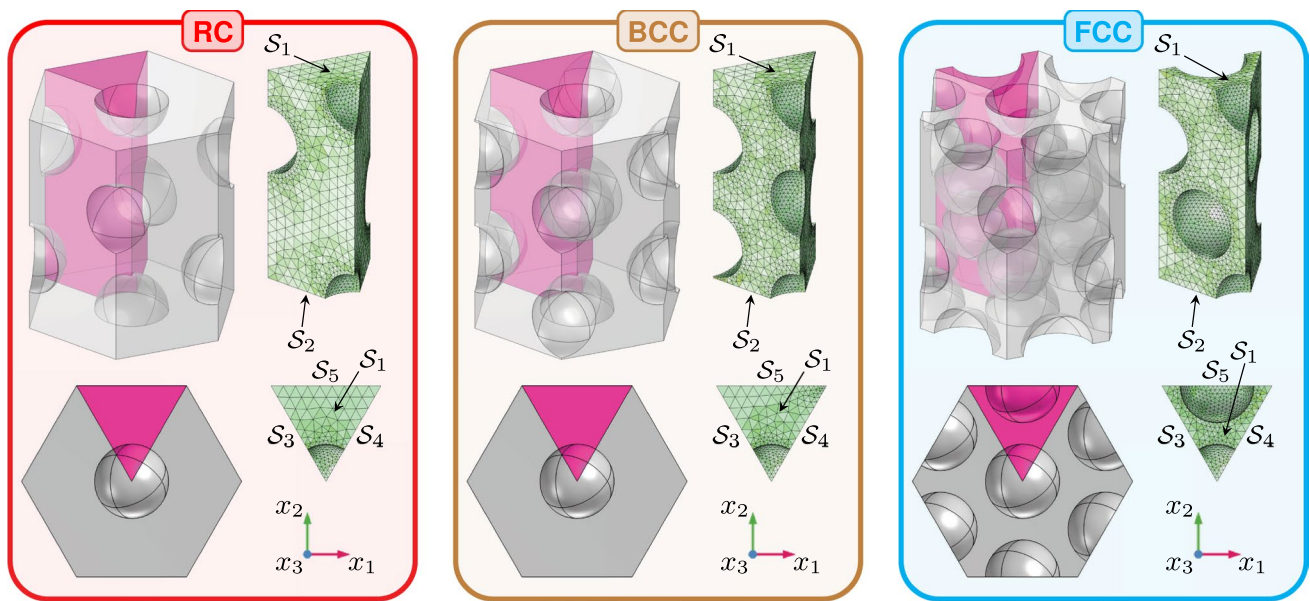


Fig. 10 Hexagonal prismatic unit cells for materials with spherical pores (quasi-isometric and top views for the RC, BCC, and FCC arrangement of pores) with FE-meshed representative segments sliced out by the planes of symmetry

and 10). On the other hand, when the cell deformation is considered, the pores inside the cell are deformed as well and the average strain $\langle \epsilon_{ij} \rangle$ cannot be calculated solely from the deformation of the solid part. One way to circumvent this is to mesh and model the pore spaces too, and then treat them as very soft inclusions, although this approach would not be efficient, and is not necessary nor applied here, because in the numerical experiments described below, the overall deformation of the cell is fixed (assumed), and thus, at least its relevant component $\bar{\epsilon}_0$ is known a priori. In this work, all finite-element calculations were performed with COMSOL Multiphysics, assuming $\bar{\epsilon}_0 = -0.001$. The fixed deformation is imposed onto a unit cell, or rather onto the appropriate representative slice of it, through boundary conditions defining (or blocking) normal displacements u_n of individual flat boundaries $\mathcal{S}_1, \mathcal{S}_2, \dots, \mathcal{S}_5$ indicated in Figs. 9 and 10. These boundary conditions will be specified in the following sections for three kinds of numerical homogenisation experiments: (i) the hydrostatic compression (Sect. 3.3)—to determine \bar{K} , (ii) the isochoric deformation (Sect. 3.4)—to determine \bar{G}_e or \bar{G}_d , and (iii) the uniaxial compression (Sect. 3.5)—to determine \bar{E}_e or \bar{E}_d . In all calculations presented below, the solid Young’s modulus $E_m = 2.3$ GPa and Poisson’s ratio $\nu_m = 0.35$ are assumed. These values agree with the results of experiments carried out on solid samples and reported in Sect. 2.2, and with the data found in the literature [51].

3.3 Hydrostatic compression

The hydrostatic compression means that $\langle \epsilon_{11} \rangle = \langle \epsilon_{22} \rangle = \langle \epsilon_{33} \rangle = \bar{\epsilon}_0 < 0$, and the overall states of strains and stresses are

$$\langle \epsilon_{ij} \rangle = \begin{bmatrix} \bar{\epsilon}_0 & 0 & 0 \\ 0 & \bar{\epsilon}_0 & 0 \\ 0 & 0 & \bar{\epsilon}_0 \end{bmatrix}, \quad \langle \sigma_{ij} \rangle = \begin{bmatrix} \langle \sigma_{33} \rangle & 0 & 0 \\ 0 & \langle \sigma_{33} \rangle & 0 \\ 0 & 0 & \langle \sigma_{33} \rangle \end{bmatrix}, \quad (19)$$

where the sign of the resulting averaged stresses $\langle \sigma_{11} \rangle = \langle \sigma_{22} \rangle = \langle \sigma_{33} \rangle$ is the same as that of $\bar{\epsilon}_0$. This state of deformation can be realised for the FE-meshed segments of the cubic cells shown in Fig. 9, by applying the following conditions on the normal displacements of their walls: $u_n(\mathcal{S}_1) = u_n(\mathcal{S}_5) = \bar{\epsilon}_0/(L_e/2)$ and $u_n(\mathcal{S}_2) = u_n(\mathcal{S}_3) = u_n(\mathcal{S}_4) = 0$. The bulk modulus is determined as

$$\bar{K} = \frac{\langle \sigma_{33} \rangle}{3\langle \epsilon_{33} \rangle} = \frac{f_m \langle \sigma_{33} \rangle_m}{3\bar{\epsilon}_0}. \quad (20)$$

Note that this formula can also be used to calculate \bar{K} from the numerical hydrostatic compression of the hexagonal prism segment (see Fig. 10), which is accomplished by applying the following normal displacements to the respective faces of the segment: $u_n(\mathcal{S}_1) = \bar{\epsilon}_0/L_d$ and $u_n(\mathcal{S}_5) = \bar{\epsilon}_0/(L_e/\sqrt{2})$, and $u_n(\mathcal{S}_2) = u_n(\mathcal{S}_3) = u_n(\mathcal{S}_4) = 0$. Although $\langle \sigma_{33} \rangle_m$ in Eq. (20) is calculated from different

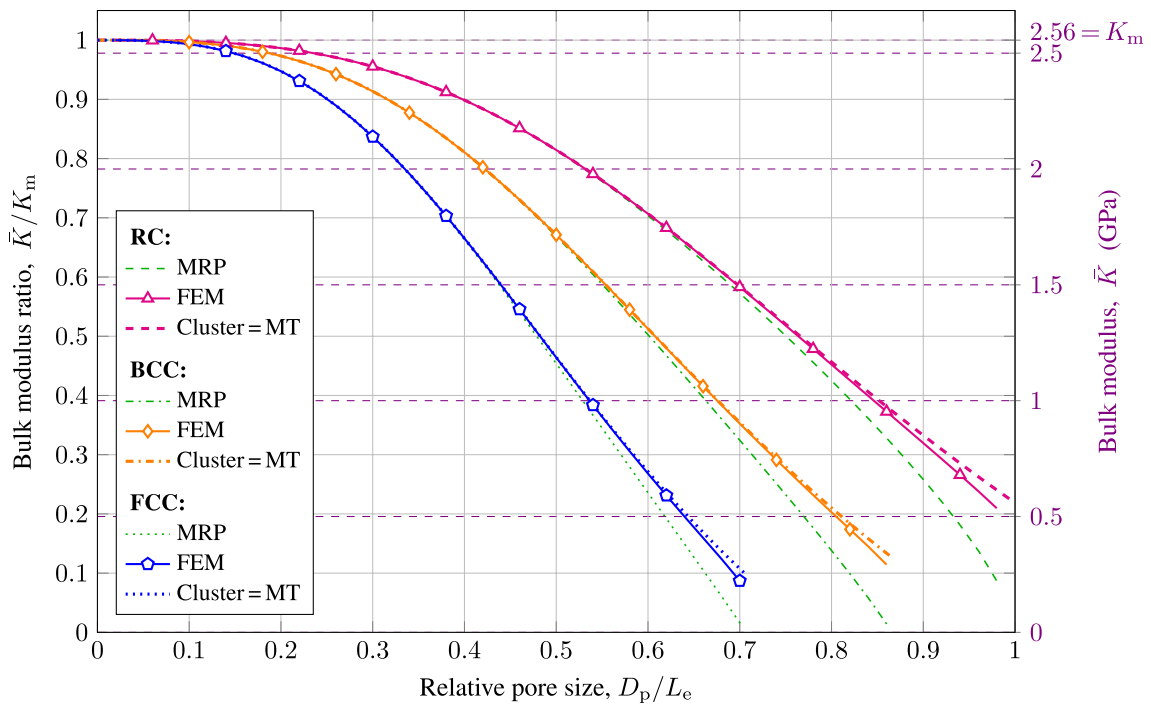


Fig. 11 The bulk moduli of materials with the RC, BCC, or FCC arrangements of spherical pores

geometries, so with different FE meshes, the bulk moduli are essentially the same.

Figure 11 compares the results of the numerical tests of hydrostatic compression performed for materials with identical spherical pores arranged according to the RC, BCC, and FCC systems. The relative size of pores D_p/L_e (with $L_e = 4$ mm) changes from zero (solid material) to the respective maximum value for which the pores are in contact but still not yet connected; see $\max(D_p/L_e)$ for RC, BCC, and FCC in Fig. 2. For numerical calculations, these values are slightly lower than the analytical maxima, so that the walls between the pores have a finite thickness everywhere. Here, the FEM results are in almost perfect agreement with the corresponding analytical predictions obtained using the mean-filed cluster approach (Cluster). Small discrepancies are observed only for the largest possible pore sizes. It has been verified that the Mori–Tanaka model (MT) provides the same bulk modulus values as the cluster approach, so the corresponding results are represented by the same curve (i.e. ‘Cluster = MT’). Furthermore, for these two analytical models, no distinction could also be made between the RC, BCC, and FCC curves when plotting the bulk modulus as a function of porosity (disregarding the fact that the maximum closed porosity values are different in each case), because even in the cluster approach, the bulk modulus is independent of the pore distribution and depends solely on the porosity value, cf. Eq. (14). On the other hand, the bulk modulus curves found by the MRP method are shown for

each case of pore distribution, since they are different and accurate only when the pores are relatively small or medium in size. Apparently, this method underestimates the values of the bulk modulus for larger pore sizes in a manner similar to that observed for Young’s modulus (see Sect. 3.5). Let us recall that the general concept of the MRP approach is the following: for each spherical inclusion (here a pore), a spherical matrix coating is assigned with the thickness specified by the mean minimum distance between the inclusions. The coating is ‘subtracted’ from the total volume fraction of the matrix, and the remaining matrix is then treated as a spherical inclusion. Next, both the coated inclusion and the ‘matrix inclusion’ are immersed in the medium of the effective properties. As a result, predictions of the MRP approach always lie between the generalised self-consistent (GSC) method and the self-consistent (SC) one. These two limit results (GSC or SC) are obtained when all matrix material is used to form a coating on one hand or when there is no coating, so the inclusions touch each other on the other hand. Thus, at variance with the cluster model, we may call the MRP approach an SC-derived method. More details on the properties of the MRP estimates can be found in [17] or [18].

3.4 Isochoric deformation

The shear moduli can be determined by numerical isochoric deformation tests of the relevant unit cells, i.e. a

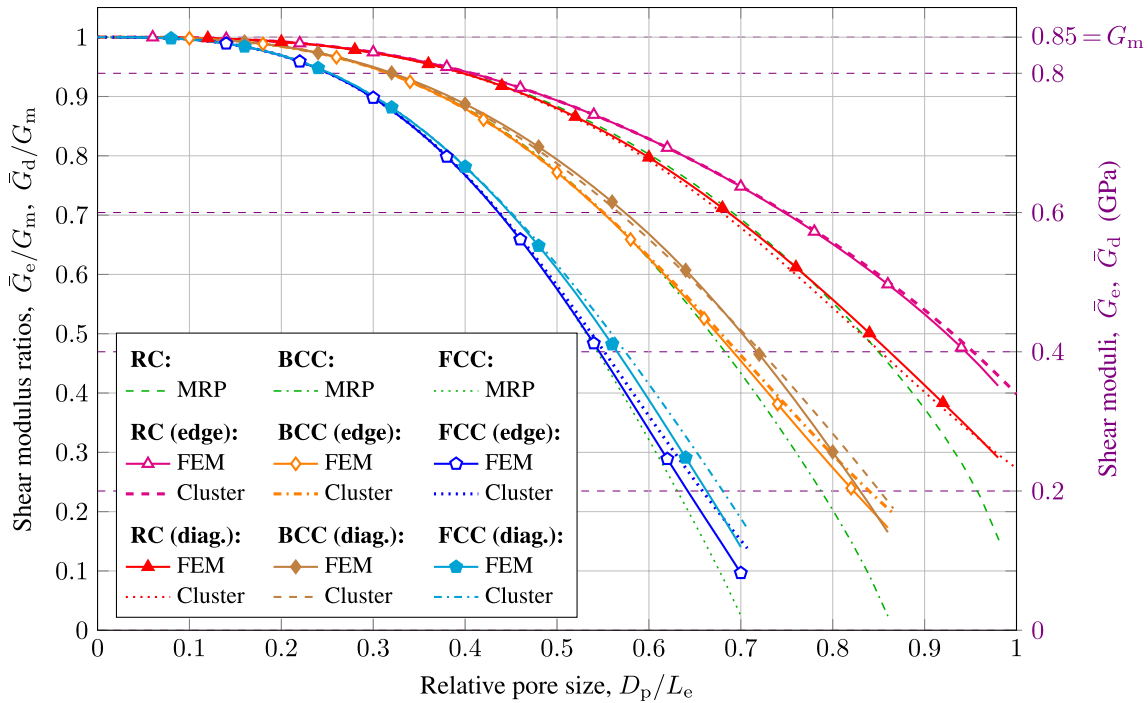


Fig. 12 The shear moduli of materials with the RC, BCC, or FCC arrangements of spherical pores

cubic cell for \bar{G}_e , or a hexagonal prism for \bar{G}_d . In such a deformation, when the unit cell is compressed (or stretched) along the x_3 -axis, i.e. $\langle \epsilon_{33} \rangle = \bar{\epsilon}_0$, then it should be properly stretched (compressed) along the remaining axes, namely $\langle \epsilon_{11} \rangle = \langle \epsilon_{22} \rangle = -\bar{\epsilon}_0/2$. The overall states of strain and stress are in the form

$$\begin{aligned}
 [\langle \epsilon_{ij} \rangle] &= \begin{bmatrix} -\bar{\epsilon}_0/2 & 0 & 0 \\ 0 & -\bar{\epsilon}_0/2 & 0 \\ 0 & 0 & \bar{\epsilon}_0 \end{bmatrix}, \\
 [\langle \sigma_{ij} \rangle] &= \begin{bmatrix} \langle \sigma_{22} \rangle & 0 & 0 \\ 0 & \langle \sigma_{22} \rangle & 0 \\ 0 & 0 & \langle \sigma_{33} \rangle \end{bmatrix},
 \end{aligned} \tag{21}$$

where the average stress $\langle \sigma_{33} \rangle$ has the same sign as $\bar{\epsilon}_0$ and the average stresses $\langle \sigma_{11} \rangle = \langle \sigma_{22} \rangle$ have the sign opposite to $\langle \sigma_{33} \rangle$. This state of isochoric deformation is realised for the representative segment of a cubic cell (see Fig. 9) by imposing the following normal displacements on surface \mathcal{S}_1 : $u_n(\mathcal{S}_1) = \bar{\epsilon}_0/(L_e/2)$, and on surface \mathcal{S}_5 : $u_n(\mathcal{S}_5) = -(\bar{\epsilon}_0/2)/(L_e/2)$. The normal displacements on the remaining planes of symmetry are blocked, i.e. $u_n(\mathcal{S}_2) = u_n(\mathcal{S}_3) = u_n(\mathcal{S}_4) = 0$. The shear modulus associated with this orientation is calculated from the averaged stress $\langle \sigma_{33} \rangle$ as

$$\bar{G}_e = \frac{\langle \sigma_{33} \rangle}{2\langle \epsilon_{33} \rangle} = \frac{f_m \langle \sigma_{33} \rangle_m}{2\bar{\epsilon}_0}. \tag{22}$$

The shear modulus \bar{G}_d is determined in the same way, but from the numerical deformation of the hexagonal prism segment, namely $\bar{G}_d = f_m \langle \sigma_{33} \rangle_m / (2\bar{\epsilon}_0)$, where $\langle \sigma_{33} \rangle_m$ is the averaged stress of the representative segment of a hexagonal prism (see Fig. 10), for which the isochoric state of strain and stress (21) is accomplished by imposing the following normal displacements on surface \mathcal{S}_1 : $u_n(\mathcal{S}_1) = \bar{\epsilon}_0/L_d$, and on surface \mathcal{S}_5 : $u_n(\mathcal{S}_5) = -(\bar{\epsilon}_0/2)/(L_e/\sqrt{2})$, while blocking the normal displacements of the bottom surface and symmetry planes, i.e. $u_n(\mathcal{S}_2) = u_n(\mathcal{S}_3) = u_n(\mathcal{S}_4) = 0$.

Figure 12 compares the shear moduli calculated using the FEM and cluster approach for three pore arrangements (RC, BCC, and FCC) and both orientations. The difference $\bar{G}_e - \bar{G}_d$ is positive and significant only for materials with (larger) pores in the RC arrangement, while negative and small for the BCC and FCC arrangements. The analytical predictions by the cluster method are in general accurate when compared to the FEM results, but the accuracy is lost for larger pores in the BCC or FCC arrangements, where the discrepancies become comparable to the differences between \bar{G}_e and \bar{G}_d . The reason for this discrepancy is probably similar to that discussed in the case of Young’s modulus predictions (see Sect. 3.5), i.e., a locally non-linear buckling-like deformation of very thin walls separating large pores. Finally, the results by

the MRP method are also provided for each pore arrangement. They correctly predict \bar{G}_e for small and medium pores in the BCC and FCC arrangements, and \bar{G}_d in the RC case. Note that the MRP model delivers isotropic overall properties, i.e., $\bar{G}_e = \bar{G}_d$, albeit different for each unit cell geometry, since the thickness of pore coating, defined within the method basing on the mean minimum distances between the pores, varies between RC, BCC, and FCC unit cells. The MRP estimate of the shear modulus is in a better agreement with the smaller of the two shear moduli \bar{G}_e and \bar{G}_d obtained for each of the three cubic arrangements. The shear modulus is underestimated by the MRP method for larger volume fraction of pores as compared to the FE calculations, consistently with the limitations observed for the self-consistent model, which is known to deliver positive stiffness only up to 50% of porosity [41].

3.5 Uniaxial compression or tension

When three independent mechanical constants for materials with cubic symmetry, e.g. \bar{G}_e , \bar{G}_d , and \bar{K} , are known, all alternative material constants can be determined from them; in particular, Young’s moduli and Poisson’s ratios can be calculated from (17) and (18), respectively. On the other hand, the most common mechanical test is uniaxial tension or compression, and in this study, such experimental tests were performed on all 3D printed solid cylinders and porous samples to measure their effective Young’s moduli (see Sect. 2.2). Acting consistently, the corresponding virtual experiments, i.e., numerical uniaxial compression tests, can be used to directly determine \bar{E}_e and \bar{E}_d , as discussed below.

The state of uniaxial compression or tension along the x_3 -axis means that $\langle \epsilon_{33} \rangle = \bar{\epsilon}_0$, where $\bar{\epsilon}_0$ is the known overall shortening (or lengthening) of the material along this direction, and the overall strain and stress are in the form

$$[\langle \epsilon_{ij} \rangle] = \begin{bmatrix} \langle \epsilon_{22} \rangle & 0 & 0 \\ 0 & \langle \epsilon_{22} \rangle & 0 \\ 0 & 0 & \bar{\epsilon}_0 \end{bmatrix}, \quad [\langle \sigma_{ij} \rangle] = \begin{bmatrix} 0 & 0 & 0 \\ 0 & 0 & 0 \\ 0 & 0 & \langle \sigma_{33} \rangle \end{bmatrix}. \tag{23}$$

The resulting strains $\langle \epsilon_{11} \rangle = \langle \epsilon_{22} \rangle$ have the sign opposite to $\bar{\epsilon}_0$, because the considered arrangements of closed pores ensure conventional behaviour of non-auxetic materials. Obviously, the resulting averaged stress $\langle \sigma_{33} \rangle$ has the same sign as $\bar{\epsilon}_0$.

To realise the uniaxial deformation of the FE-meshed segments of the cubic cells shown in Fig. 9, the normal displacements of surface \mathcal{S}_1 are specified as $u_n(\mathcal{S}_1) = \bar{\epsilon}_0/(L_e/2)$, whereas they are blocked on boundaries \mathcal{S}_2 , \mathcal{S}_3 , and \mathcal{S}_4 , i.e. $u_n(\mathcal{S}_2) = u_n(\mathcal{S}_3) = u_n(\mathcal{S}_4) = 0$. A special condition has to be applied on \mathcal{S}_5 , so that this wall moves freely along its normal as a flat surface. This can be done by applying the following

constraint: $u_n(\mathcal{S}_5) = \langle u_n(\mathcal{S}_5) \rangle_{\mathcal{S}_5}$, where $\langle \dots \rangle_{\mathcal{S}_5} = \frac{1}{S_5} \int_{\mathcal{S}_5} \dots dS$ is the averaging operator over the surface \mathcal{S}_5 . Alternatively, the same condition can be realised by requiring that normal displacements of \mathcal{S}_5 are all equal to the normal displacement at an arbitrarily chosen point \mathcal{P} on this surface, i.e. $u_n(\mathcal{S}_5) = u_n(\mathcal{P})$ for \mathcal{P} on \mathcal{S}_5 . No surface integration (averaging) is required in this case, so this approach is preferred, but should also be used with caution when performing parametric analyses where the relative pore size changes like in the numerical tests of this work. Specifically, the point \mathcal{P} should be defined, so that it *always* lies on the wall \mathcal{S}_5 when the pores in the cell are being enlarged. After performing such FEM analyses, Young’s modulus is calculated as

$$\bar{E}_e = \frac{\langle \sigma_{33} \rangle}{\langle \epsilon_{33} \rangle} = \frac{f_m \langle \sigma_{33} \rangle_m}{\bar{\epsilon}_0}. \tag{24}$$

This numerical test, and in particular the resulting normal displacement of the flat boundary \mathcal{S}_5 , can also be used to determine the corresponding Poisson’s ratio $\bar{\nu}_e = -\langle \epsilon_{22} \rangle / \bar{\epsilon}_0$, where $\langle \epsilon_{22} \rangle = u_n(\mathcal{P})/(L_e/2)$ for any point \mathcal{P} on \mathcal{S}_5 .

The same uniaxial state of strains and stresses (23) can be realised in a similar way for the segments of the hexagonal prisms shown in Fig. 10. Due to different dimensions of the cell, the normal displacement on the upper surface is specified as $u_n(\mathcal{S}_1) = \bar{\epsilon}_0/L_d$, but the boundary conditions on the remaining surfaces are the same as for the the cubic cell segment described above. The Young’s modulus for this orientation, i.e. along the diagonal of the original cube, is determined from the averaged stresses of the hexagonal prism segment as $\bar{E}_d = f_m \langle \sigma_{33} \rangle_m / \bar{\epsilon}_0$, and the corresponding Poisson’s ratio as $\bar{\nu}_d = -\langle \epsilon_{22} \rangle / \bar{\epsilon}_0$, where $\langle \epsilon_{22} \rangle = u_n(\mathcal{P})/(L_h \sqrt{3}/2) = u_n(\mathcal{P})/(L_e/\sqrt{2})$ for any point \mathcal{P} on \mathcal{S}_5 .

The results of direct numerical tests for \bar{E}_e and \bar{E}_d are identical to those calculated indirectly from formulae (17), which confirms the entire numerical homogenisation procedure. Figures 13, 14 and 15 compare the effective Young’s moduli determined for two orientations of the porous materials with spherical pores in the RC, BCC, and FCC arrangements, respectively. In each graph, the results of numerical homogenisation by FEM are confronted with the analytical calculations for the cluster associated with the respective unit cell, as well as with the experimental results measured for several 3D printed samples discussed in Sects. 2.1 and 2.2. Recall that the experimental Young’s moduli are plotted for the relative pore diameter values, D_p/L_e , determined for the *actual* pore sizes listed in Table 3. Additional analytical results are presented in each graph for the Voigt upper bound (Voigt), self-consistent model (SC), Mori–Tanaka model (MT), and the method of morphologically representative pattern (MRP).

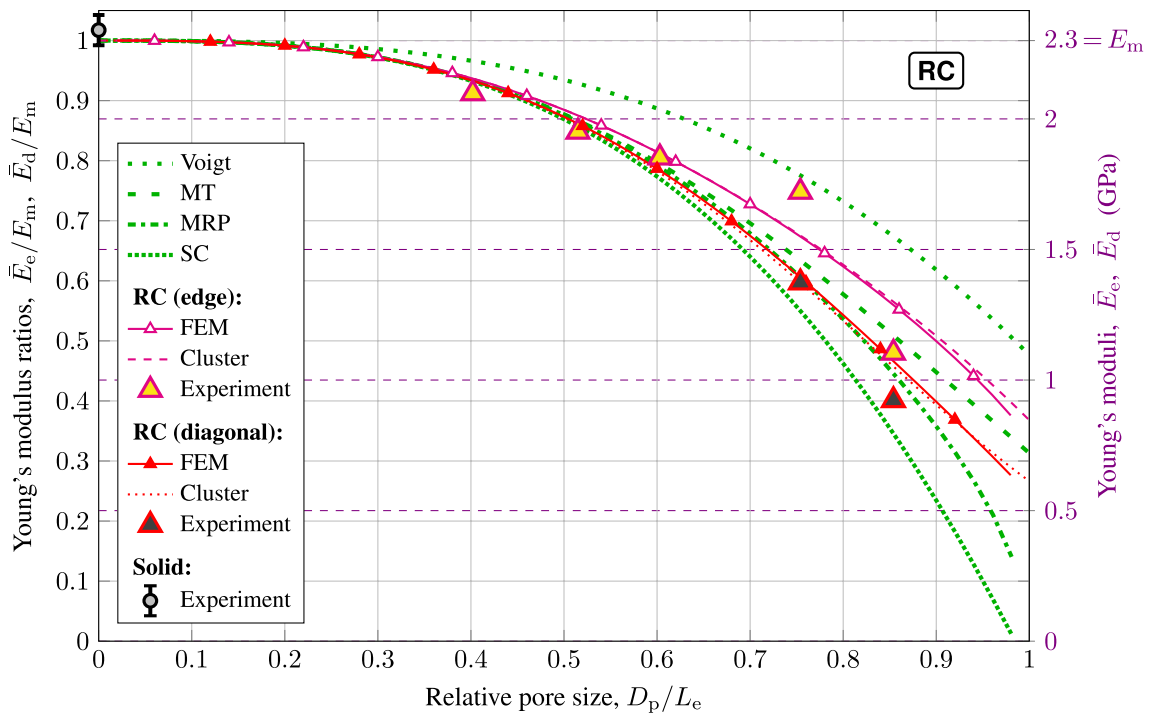


Fig. 13 Young's moduli of materials with spherical pores arranged according to the RC system

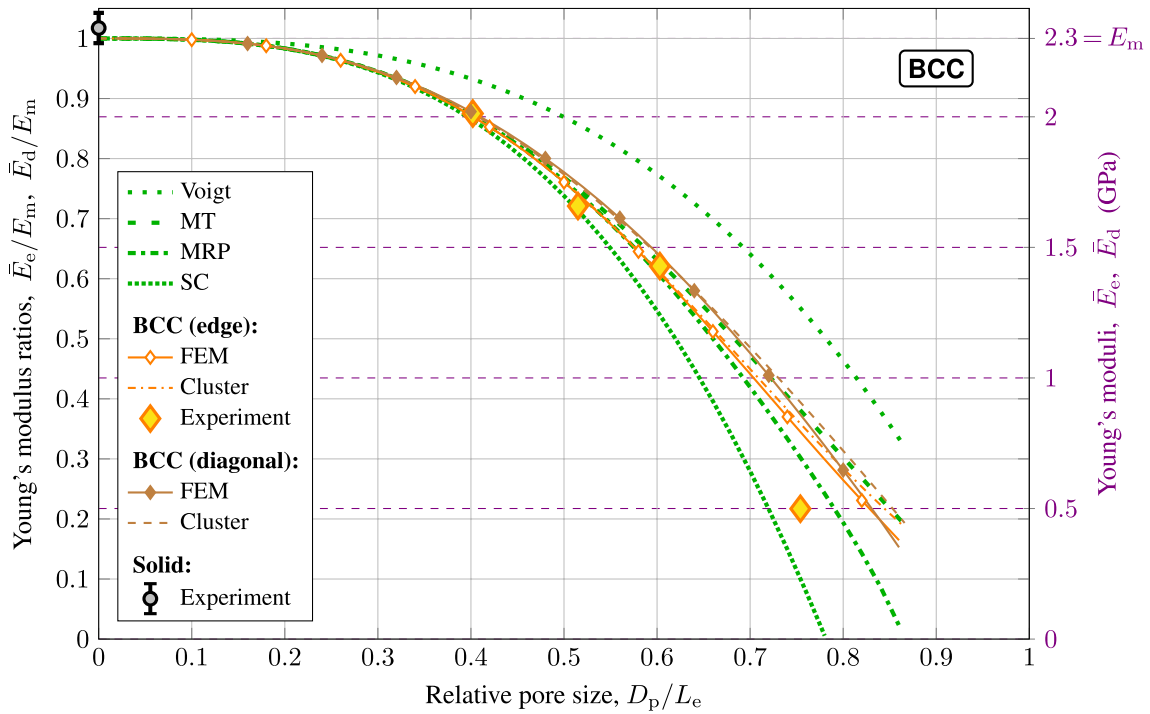


Fig. 14 Young's moduli of materials with spherical pores arranged according to the BCC system

In general, the agreement between the FEM and cluster calculations is very good and the discrepancy is clearly visible only when the pores are relatively large.

This discrepancy is due to deformation of thin walls separating large pores which is demonstrated in Fig. 16 for the FCC case—see in particular the detail of the deformed

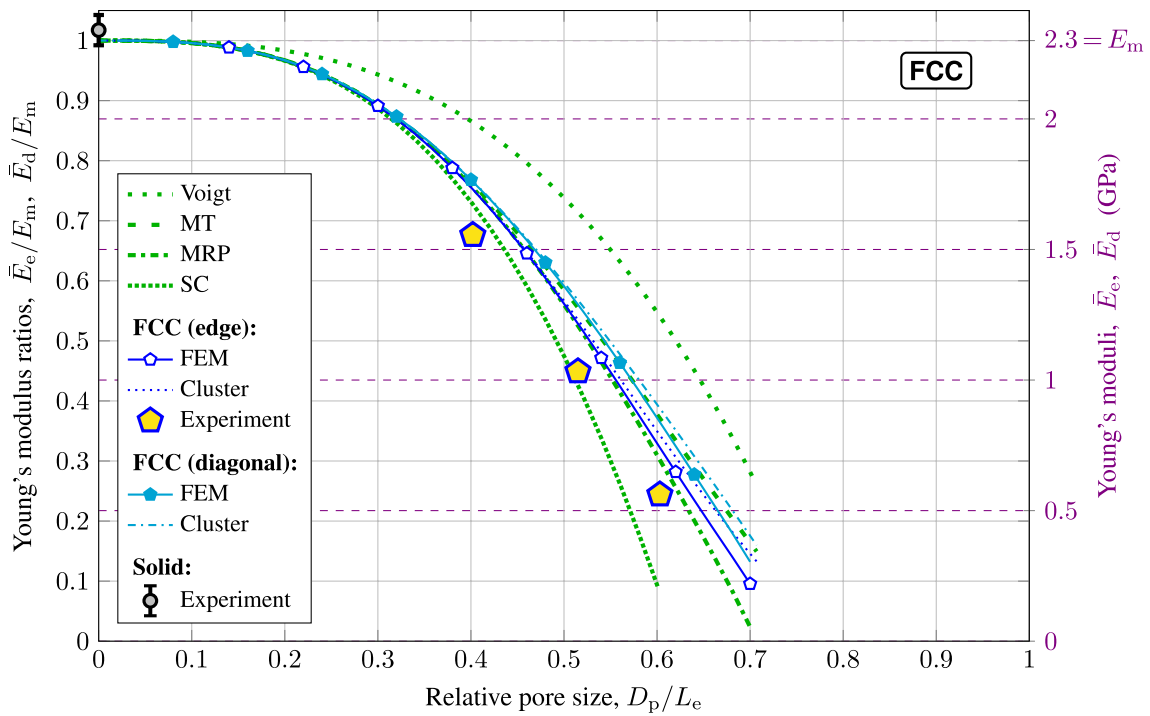


Fig. 15 Young’s moduli of materials with spherical pores arranged according to the FCC system

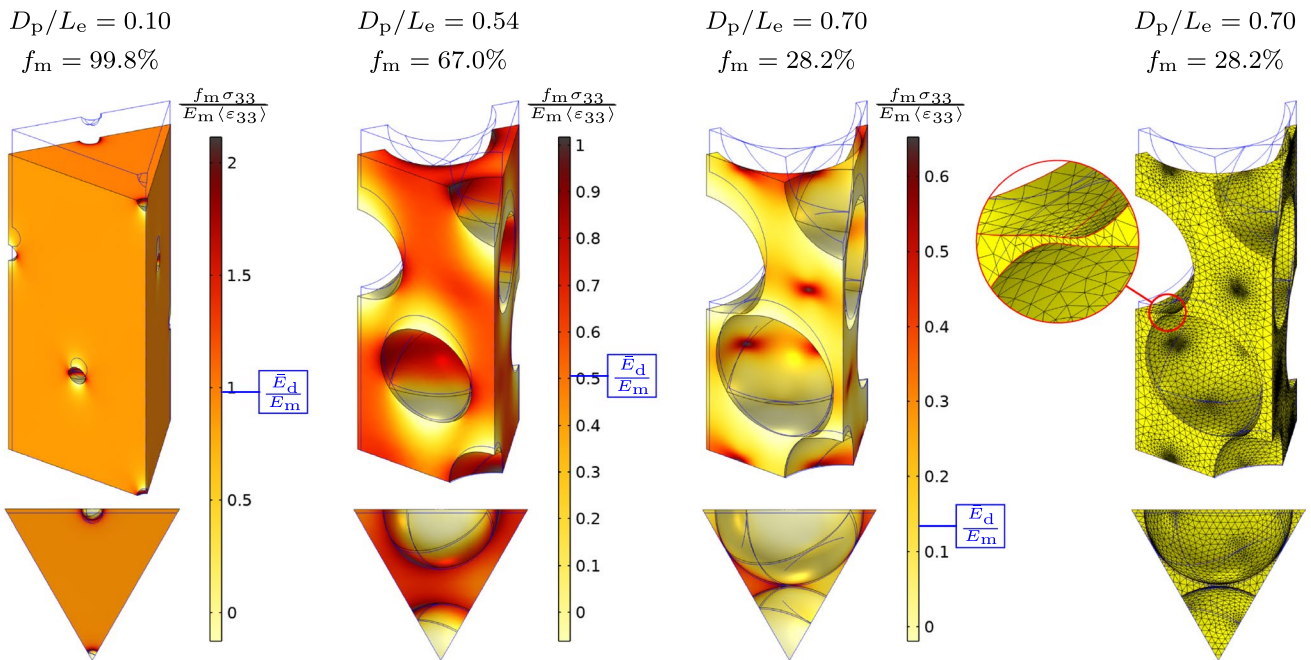


Fig. 16 Normalised stress and scaled deformation of the axially compressed representative segments of hexagonal prisms with spherical pores in the FCC arrangement—for various pore sizes and solid volume fractions

mesh for $D_p/L_e = 0.7$. The buckling-like deformation of thin walls is only captured by the FE solution and makes such a porous material—with locally very thin walls—slightly softer than the cluster model is able to predict.

Note that the stress σ_{33} shown in Fig. 16 is normalised, i.e. divided by $\bar{\epsilon}_0 E_m/f_m$, and its sign is the same as $\bar{\epsilon}_0$ almost everywhere, except for small regions at the top or bottom of the pores. Moreover, when the pores are small, e.g.

for $D_p/L_e \leq 0.1$, the normalised stress is the same almost everywhere and close to the averaged value, i.e. the ratio \bar{E}_d/E_m . For larger pores, the stress distribution is more complex, cf. the results for $D_p/L_e = 0.54$ and $D_p/L_e = 0.70$ in Fig. 16.

A significant difference between \bar{E}_e and \bar{E}_d is shown only by materials with the RC arrangement of pores, see Fig. 13, and only for larger pores. In this case, the material is stiffer along the cube's edge, i.e. $\bar{E}_e - \bar{E}_d > 0$, because even with very large pores, there is a continuous solid core along this direction. On the other hand, this difference is negative when the pores are arranged according to the BCC or FCC system (cf. \bar{E}_e and \bar{E}_d in Figs. 14 and 15), and rather insignificant, in particular in the BCC case. All these observations are consistent with the fact that porous materials based on the RC system have stronger anisotropy than in the other cases; cf. Fig. 8.

As for other analytical models, recall that these models are inherently isotropic and do not distinguish between the two orientations (i.e. along the edge or the diagonal of the cubic unit cell). The Voigt model shows the upper bound correctly,² but with quite a large margin. The self-consistent model generally gives lower bound predictions that are accurate for relatively small pores, but fail equally as the void fraction increases. Predictions by the Mori–Tanaka model are quite accurate and are somewhat in between the results obtained for \bar{E}_e and \bar{E}_d using the FEM or cluster approach. Therefore, this model is very useful when the spherical pores are arranged in the BCC or FCC system, since the difference between \bar{E}_e and \bar{E}_d is small in these cases; see Figs. 14 and 15. The MRP model can be used to predict the 'lower' Young's modulus, that is \bar{E}_d in the RC case (see Fig. 13), but \bar{E}_e in the BCC or FCC cases (see Figs. 14 and 15); however, it clearly underestimates the values for larger pores.

Young's moduli measured on 3D printed samples generally confirm the predictions of the FE and cluster methods, although the differences between the corresponding numerical and analytical calculations are very small and negligible when compared to the discrepancies with the experimental results. As we have a full control on the input data (i.e., solid phase properties, pore geometry, and boundary conditions) used in the numerical calculations, there is much more uncertainty when interpreting the experimental data. Thus, while the comparison between the high fidelity FE results and mean-field model estimates verifies very well the assumptions used to formulate analytical models, the comparison with a physical experiment is more difficult. Therefore, to some extent, the observed differences between the mean-field model predictions verify in fact the quality

and repeatability of the 3D printed samples. Recall that the shapes of the pores in the samples are slightly distorted (see Fig. 4) and their real diameters were taken as averaged values. Moreover, all calculations were made for $E_m = 2.3$ GPa and $\nu_m = 0.35$, which are the averages of measurements on three solid samples, assuming that the 3D printed material of the matrix is isotropic. Such geometrical and material imperfections (see Fig. 4) may result in a more substantial local loss of response stability leading to a locally non-linear sample response, which is also observed in the numerical analyses, although to a much lesser extent. All of this explains the overall acceptable discrepancy between predictions and measurements, and the experimental validation seems to be satisfactory, especially in terms of qualitative observations. In particular, it is important that the difference between \bar{E}_e and \bar{E}_d for the RC system was captured by the experiments (see Fig. 13). For yet another comparison, all experimental results along with the corresponding predictions by the FEM and cluster approach are plotted together in Fig. 17 with respect to the porosity and solid volume fraction. This graph clearly shows that the porosity has a major and primary effect on stiffness reduction, while the effect of pore arrangement is secondary. It is also clear that for the same porosity, the Young's moduli \bar{E}_d for the RC system and \bar{E}_e for the BCC and FCC systems are quite similar, while they more significantly differ from \bar{E}_e found for the RC system. Recall, however, that the highest porosities available to these systems of closed, i.e. non-overlapping spherical pores are substantially different. Regarding the measurement results for the 3D printed samples, the primary effect of porosity was satisfactorily observed in the experiment, while the secondary effect of pore distribution could only be assessed qualitatively, based on the differences between \bar{E}_d and \bar{E}_e (cf. the corresponding black and yellow triangular markers in Fig. 17), since the measurement error of Young's modulus is of the order of the secondary effect.

4 Conclusions

The effect of pore distribution on the anisotropic elastic properties of porous materials produced by additive manufacturing has been analysed. In particular, three periodic arrangements of closed pores, based on the well-known cubic symmetry systems, RC, BCC, and FCC, have been comprehensively studied by means of experimental analysis, numerical and mean-field modelling.

The mean-field estimates by the interaction 'cluster' model, initially proposed by [29] for the general case of a multiphase particulate composite, have been specified here for porous materials as a relevant micromechanical approach. The closed-form formulas for three independent cubic elastic moduli (14)–(16) have been derived assuming

² Note that the lower bound by the simple Reuss model is not relevant here as it delivers zero stiffness for porous materials.

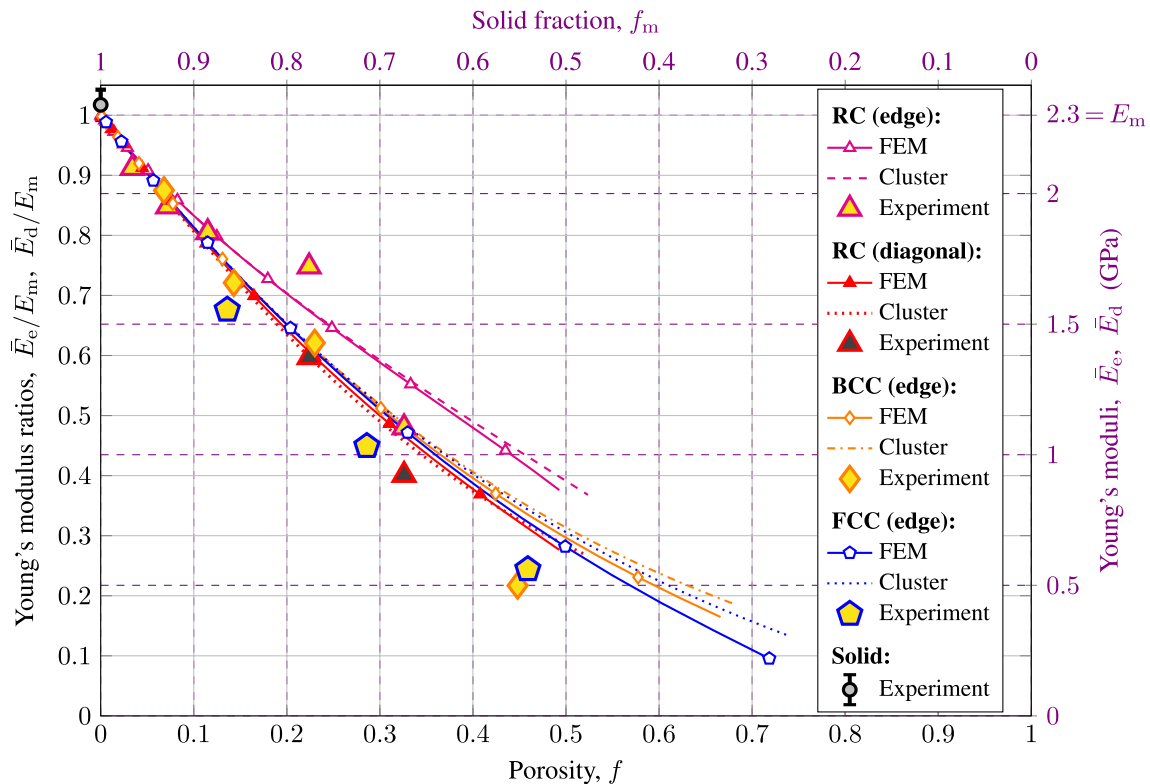


Fig. 17 Young's moduli vs. porosity and solid volume fraction for solid and porous materials with RC, BCC, and FCC arrangements of spherical pores

sufficiently large cluster size to reach the model convergence. The model assumes isotropy of the solid phase and spherical shape of pores. It should be noted that although the cluster model is used here for the relatively simple cubic anisotropy, its formulation admits arbitrary periodic space distribution of pores with different sizes, which may lead to arbitrary anisotropy of the effective elastic stiffness tensor.

The proposed mean-field modelling scheme has been verified by a numerical homogenisation procedure performed on the unit cells. Excellent agreement between analytical estimates and numerical predictions has been observed for a large range of porosities (i.e., pore sizes) and all considered microstructures (i.e., pore distributions). Moreover, in spite of its relative simplicity, the 'cluster' model is able to correctly describe the cubic anisotropy of effective elastic properties, resulting from the periodic distribution of pores, as opposed to other mean-field models. This proves the validity of the applied micro–macro transition scheme.

The obtained results allow us to positively answer two questions raised in the introduction. We have demonstrated that there is a non-negligible influence of morphological features on the developed anisotropy degree of the effective elastic stiffness of a porous material even if the solid phase is isotropic and pores are spherical. We have also shown that the mean-field cluster model is a computationally efficient

tool which correctly describes this effect, at least for the analysed cases.

The mean-field estimates and numerical predictions of the effective Young's modulus have also been confronted with the results of uniaxial compression experiments performed on 3D printed cylindrical samples with varying pore sizes and the three cubic geometries. The measurement and modelling results are in good agreement in terms of the quantitative assessment of the primary effect related to porosity (or relative pore size). Qualitative compliance is also observed with respect to the anisotropy of the tensile Young's modulus. The quantitative assessment of the secondary effect of pore distribution on the fabricated samples is more challenging, mainly due to inherent inaccuracy of 3D printed geometries and possible variation of solid properties within the samples. Nevertheless, the use of low-cost additive manufacturing techniques to prototype porous and composite materials for testing mean-field approaches, useful in microstructure optimisation, can be recommended and is, indeed, a promising methodology.

In further research, the cluster model should be verified for more complex pore distributions (of lower symmetry and/or different sizes of pores), which will require usage of the multi-family model variant [29]. Moreover, the possibility of its application to estimate the yield stress

or strength of the porous material should be investigated. When it comes to applying the FDM technique for the purpose of mean-field model validation, the use of more accurate printing techniques that enable an enhanced control of the sample microstructure should be considered.

Author contributions KK-G (corresponding author): conceptualization; funding acquisition; methodology; software; supervision; validation; visualisation; writing—original draft; writing—review & editing. MM: conceptualization; resources; data curation; investigation; writing—review & editing. KB: software; visualisation. MM: software; visualisation. KCO: investigation; data curation; methodology; writing - review & editing. TGZ: conceptualization; resources; funding acquisition; methodology; validation; visualisation; software; writing—original draft; writing—review & editing.

Funding This research was partially supported by two projects financed by the National Science Center (NCN), Poland, under Grant Agreements: No. 2016/23/B/ST8/03418 (K. Kowalczyk-Gajewska, K. Bieniek, M. Maj, M. Majewski) and No. 2021/41/B/ST8/04492 (T. G. Zieliński, K. C. Opiela).

Data availability Data will be made available on request.

Declarations

Conflict of interest The authors have no competing interests to declare that are relevant to the content of this article.

Ethical approval The authors state that the research was conducted according to ethical standards. This article does not contain any studies with human participants or animals performed by any of the authors.

Open Access This article is licensed under a Creative Commons Attribution 4.0 International License, which permits use, sharing, adaptation, distribution and reproduction in any medium or format, as long as you give appropriate credit to the original author(s) and the source, provide a link to the Creative Commons licence, and indicate if changes were made. The images or other third party material in this article are included in the article's Creative Commons licence, unless indicated otherwise in a credit line to the material. If material is not included in the article's Creative Commons licence and your intended use is not permitted by statutory regulation or exceeds the permitted use, you will need to obtain permission directly from the copyright holder. To view a copy of this licence, visit <http://creativecommons.org/licenses/by/4.0/>.

References

- Torquato S. Random heterogeneous materials. Microstructure and Macroscopic Properties: Springer; 2002.
- Biot MA. The theory of propagation of elastic waves in a fluid-saturated porous solid. *J Acoust Soc Am*. 1956;28(2):168–91. <https://doi.org/10.1121/1.1908239>.
- Campoli G, Borleffs MS, Yavari SA, Wauthle R, Weinans HH, Zadpoor AA. Mechanical properties of open-cell metallic biomaterials manufactured using additive manufacturing. *Mater Des*. 2013;49:957–65. <https://doi.org/10.1016/j.matdes.2013.01.071>.
- Andersons JA, Kirpluks M, Stiebra L, Cabulis U. Anisotropy of the stiffness and strength of rigid low-density closed-cell polyisocyanurate foams. *Mater Des*. 2016;92:836–45. <https://doi.org/10.1016/j.matdes.2015.12.122>.
- Al-Maharma AY, Patil SP, Markert B. Effects of porosity on the mechanical properties of additively manufactured components: a critical review. *Mater Res Express*. 2020;7(12):1–27. <https://doi.org/10.1088/2053-1591/abcc5d>.
- Dizon JRC, Espera AH Jr, Chen Q, Advincula RC. Mechanical characterization of 3D-printed polymers. *Addit Manuf*. 2018;20:44–67. <https://doi.org/10.1016/j.addma.2017.12.002>.
- Moradi M, Aminzadeh A, Rahmatabadi D, Hakimi A. Experimental investigation on mechanical characterization of 3D printed PLA produced by fused deposition modeling (FDM). *Mater Res Express*. 2021;8(3):1–10. <https://doi.org/10.1088/2053-1591/abe8f3>.
- Mao H, Rumpler R, Gaborit M, Göransson P, Kennedy J, O'Connor D, Trimble D, Rice H. Twist, tilt and stretch: from isometric Kelvin cells to anisotropic cellular materials. *Mater Des*. 2020;193:1–15. <https://doi.org/10.1016/j.matdes.2020.108855>.
- Mao H, Rumpler R, Göransson P. A note on the linear deformations close to the boundaries of a cellular material. *Mech Res Commun*. 2021;111:1–7. <https://doi.org/10.1016/j.mechrescom.2021.103657>.
- Mueller J, Shea K. Buckling, build orientation, and scaling effects in 3D printed lattices, *Materials Today. Communications*. 2018;17:69–75. <https://doi.org/10.1016/j.mtcomm.2018.08.013>.
- Eshelby JD. The determination of the elastic field of an ellipsoidal inclusion, and related problems. *Proc Roy Soc A*. 1957;241:376–96. <https://doi.org/10.1098/rspa.1957.0133>.
- Nemat-Nasser S, Hori M. *Micromechanics: overall properties of heterogeneous materials*, North-Holland Elsevier 1999.
- Herve E, Zaoui A. n-layered inclusion-based micromechanical modelling. *Int J Engng Sci*. 1993;31:1–10. [https://doi.org/10.1016/0020-7225\(93\)90059-49](https://doi.org/10.1016/0020-7225(93)90059-49).
- Cherkaoui M, Sabar H, Berveiller M. Micromechanical approach of the coated inclusion problem and applications to composite materials. *J Eng Mater Technol*. 1994;116:274–8. <https://doi.org/10.1051/jp3:1994161>.
- Capolungo L, Cherkaoui M, Qu J. On the elastic-viscoplastic behavior of nanocrystalline materials. *Int J Plast*. 2007;23:561–91. <https://doi.org/10.1016/j.ijplas.2006.05.003>.
- Duan H, Yi X, Huang Z, Wang J. A unified scheme for prediction of effective moduli of multiphase composites with interface effects. Part I: Theoretical framework. *Mech Mater*. 2007;39:81–93. <https://doi.org/10.1016/j.mechmat.2006.02.009>.
- Marcadon V, Herve E, Zaoui A. Micromechanical modeling of packing and size effects in particulate composites. *Int J Solids Struct*. 2007;44:8213–28. <https://doi.org/10.1016/j.ijsolstr.2007.06.008>.
- Majewski M, Kurasa M, Holobut P, Kowalczyk-Gajewska K. Micromechanical and numerical analysis of packing and size effects in elastic particulate composites. *Compos B*. 2017;124:158–74. <https://doi.org/10.1016/j.compositesb.2017.05.004>.
- Vu T-S, Tran B-V, Nguyen H-Q, Chateau X. A refined morphological representative pattern approach to the behavior of poly-disperse highly-filled inclusion-matrix composites. *Int J Solids Struct*. 2023;270: 112253. <https://doi.org/10.1016/j.ijsolstr.2023.112253>.
- Ponte Castañeda P, Willis J. The effect of spatial distribution on the effective behavior of composite materials and cracked media. *J Mech Phys Solids*. 1995;43(12):1919–51. [https://doi.org/10.1016/0022-5096\(95\)00058-Q](https://doi.org/10.1016/0022-5096(95)00058-Q).
- Ma H, Hu G, Huang Z. A micromechanical method for particulate composites with finite particle concentration. *Mech Mater*. 2004;36(4):359–68. [https://doi.org/10.1016/S0167-6636\(03\)00065-6](https://doi.org/10.1016/S0167-6636(03)00065-6).

22. Li D, Hu G-K. Effective viscoelastic behavior of particulate polymer composites at finite concentration. *Appl Math Mech-Engl Ed.* 2007;28(3):297–307. <https://doi.org/10.1007/s10483-007-0303-1>.
23. Vilchevskaya E, Kushch V, Kachanov M, Sevostianov I. Effective properties of periodic composites: Irrelevance of one particle homogenization techniques. *Mech Mater.* 2021;159: 103918. <https://doi.org/10.1016/j.mechmat.2021.103918>.
24. Sangani AS, Lu W. Elastic coefficients of composites containing spherical inclusions in a periodic array. *J Mech Phys Solids.* 1987;35(1):1–21. [https://doi.org/10.1016/0022-5096\(87\)90024-X](https://doi.org/10.1016/0022-5096(87)90024-X).
25. Rodin GJ. The overall elastic response of materials containing spherical inhomogeneities. *Int J Solids Struct.* 1993;30(14):1849–63. [https://doi.org/10.1016/0020-7683\(93\)90221-R](https://doi.org/10.1016/0020-7683(93)90221-R).
26. Nemat-Nasser S, Iwakuma T, Hejazi M. On composites with periodic structure. *Mech Mater.* 1982;1(3):239–67. [https://doi.org/10.1016/0167-6636\(82\)90017-5](https://doi.org/10.1016/0167-6636(82)90017-5).
27. Schjødt-Thomsen J, Pyrz R. Cubic inclusion arrangement: effect on stress and effective properties. *Comput Mater Sci.* 2005;34(2):129–39. <https://doi.org/10.1016/j.commatsci.2004.12.061>.
28. Kushch VI, Mogilevskaya SG, Stolarski HK, Crouch SL. Evaluation of the effective elastic moduli of particulate composites based on Maxwell's concept of equivalent inhomogeneity: microstructure-induced anisotropy. *J Mech Mater Struct.* 2013;8(5–7):283–303. <https://doi.org/10.2140/jomms.2013.8.283>.
29. Molinari A, El Mouden M. The problem of elastic inclusions at finite concentration. *Int J Solids Struct.* 1996;33:3131–50. [https://doi.org/10.1016/0020-7683\(95\)00275-8](https://doi.org/10.1016/0020-7683(95)00275-8).
30. El Mouden M, Molinari A. Thermoelastic properties of composites containing ellipsoidal inhomogeneities. *J Therm Stress.* 2000;23:233–55. <https://doi.org/10.1080/014957300280425>.
31. FreeCAD, FreeCAD (version 0.20). <https://www.freecadweb.org/>. Accessed 1 Mar 2023.
32. Ngo TD, Kashani A, Imbalzano G, Nguyen KTQ, Hui D. Additive manufacturing (3D printing): a review of materials, methods, applications and challenges. *Compos B Eng.* 2018;143:172–96. <https://doi.org/10.1016/j.compositesb.2018.02.012>.
33. Nowak M, Maj M. Determination of coupled mechanical and thermal fields using 2D digital image correlation and infrared thermography: numerical procedures and results. *Arch Civ Mech Eng.* 2018;18(2):630–44. <https://doi.org/10.1016/j.acme.2017.10.005>.
34. Musiał S, Maj M, Urbański L, Nowak M. Field analysis of energy conversion during plastic deformation of 310s stainless steel. *Int J Solids Struct.* 2022;238: 111411. <https://doi.org/10.1016/j.ijsolstr.2021.111411>.
35. Mercier S, Molinari A, El Mouden M. Thermal conductivity of composite material with coated inclusions: applications to tetragonal array of spheroids. *J Appl Phys.* 2000;87:3511. <https://doi.org/10.1063/1.372374>.
36. Kowalczyk-Gajewska K, Majewski M, Mercier S, Molinari A. Mean field interaction model accounting for the spatial distribution of inclusions in elastic-viscoplastic composites. *Int J Solids Struct.* 2021;224: 111040. <https://doi.org/10.1016/j.ijsolstr.2021.111040>.
37. Bieniek K, Majewski M, Holobut P, Kowalczyk-Gajewska K. Composite anisotropy induced by the spatial distribution of particles: the cluster model and numerical homogenization, submitted 2023.
38. Zeller R, Dederichs P. Elastic constant of polycrystals. *Phys Status Solidi B.* 1973;55:831–42. <https://doi.org/10.1002/pssb.2220550241>.
39. Forte S, Vianello M. Symmetry classes for elasticity tensors. *J Elast.* 1996;43:81–108. <https://doi.org/10.1007/BF00042505>.
40. Kowalczyk-Gajewska K. Estimation of overall properties of random polycrystals with the use of invariant decompositions of Hooke's tensor. *Int J Solids Struct.* 2012;49:3022–37. <https://doi.org/10.1016/j.ijsolstr.2012.06.002>.
41. Benveniste Y. A new approach to the application of Mori-Tanaka's theory in composite materials. *Mech Mater.* 1987;6(2):147–57. [https://doi.org/10.1016/0167-6636\(87\)90005-6](https://doi.org/10.1016/0167-6636(87)90005-6).
42. Sevostianov I, Kachanov M. On some controversial issues in effective field approaches to the problem of the overall elastic properties. *Mech Mater.* 2014;69(1):93–105. <https://doi.org/10.1016/j.mechmat.2013.09.010>.
43. Jiménez Segura N, Pichler BL, Hellmich C. Concentration tensors preserving elastic symmetry of multiphase composites. *Mech Mater.* 2023;178: 104555. <https://doi.org/10.1016/j.mechmat.2023.104555>.
44. Rychlewski J. CEIINOSSSTTUV. Mathematical structure of elastic bodies, Tech. Rep. 217, Inst. Mech. Probl. USSR Acad. Sci., Moskva, in Russian, 1983. English Translations by A. Ziółkowski: Library of Applied Mechanics, Institute of Fundamental Technological Research, Polish Academy of Sciences, ISBN: 978-83-65550-45-3, Warsaw, 2023.
45. Ostrowska-Maciejewska J, Rychlewski J. Generalized proper states for anisotropic elastic materials. *Arch Mech.* 2001;53(4–5):501–18.
46. Kouznetsova V, Brekelmans W, Baaijens F. An approach to micro-macro modeling of heterogeneous materials. *Comput Mech.* 2001;27:37–48. <https://doi.org/10.1007/s004660000212>.
47. Pierard O, Lorca J, Segurado J, Doghri I. Micromechanics of particle-reinforced elasto-viscoplastic composites: finite element simulations versus affine homogenization. *Int J Plast.* 2007;23:1041–60. <https://doi.org/10.1016/j.ijplas.2006.09.003>.
48. Kurska M, Kowalczyk-Gajewska K, Lewandowski M, Petryk H. Elastic-plastic properties of metal matrix composites: Validation of mean-field approaches. *Eur J Mech A Solids.* 2018;68:53–66. <https://doi.org/10.1016/j.euromechsol.2017.11.001>.
49. Mercier S, Kowalczyk-Gajewska K, Czarnota C. Effective behavior of composites with combined kinematic and isotropic hardening based on additive tangent Mori-Tanaka scheme. *Compos B Eng.* 2019;174:107052. <https://doi.org/10.1016/j.compositesb.2019.107052>.
50. Majewski M, Wichrowski M, Holobut P, Kowalczyk-Gajewska K. Shape and packing effects in particulate composites: micro-mechanical modelling and numerical verification. *Arch Civ Mech Eng.* 2022;22:86. <https://doi.org/10.1007/s43452-022-00405-9>.
51. Zou R, Xia Y, Liu S, Hu P, Hou W, Hu Q, Shan C. Isotropic and anisotropic elasticity and yielding of 3D printed material. *Compos B Eng.* 2016;99:506–13. <https://doi.org/10.1016/j.compositesb.2016.06.009>.

Publisher's Note Springer Nature remains neutral with regard to jurisdictional claims in published maps and institutional affiliations.